CHAPTER - 3

Metal oxide nanoparticles

3.1. Nanocrystalline copper oxide (CuO)

3.1.1. Introduction

Copper oxide is widely applied in different technological fields and scientific areas because of its interesting characteristics such as low cost, easy availability, non toxicity and ease of preparation [Pendashteh *et al.* (2013)]. Copper oxide nanoparticles possess unique properties such as highly reactive surface faces, homogeneity and large surface area [Hong *et al.* (2002)]. As nanocrystalline copper oxide is a p-type semiconductor with narrow band gap (1.2 eV), it is generally used in variety of applications for example solar cells, high temperature superconductors, field emission devices, catalysis, photo-catalysis, batteries, lithium-ion electrode materials, ceramic pigments, humidity and gas sensors etc. [Yang *et al.* (2011), Wongpisutpaisan *et al.* (2011), Ren *et al.* (2009), Hosny and Zoromba (2012)]. Some authors have reported [Ren *et al.* (2009), Baek and An (2011)] that nanocrystalline copper oxide also exhibits antimicrobial activity against *Escherichia coli*, *Bacillus subtilis*, and *Staphylococcus aureus*. Nanocrystalline copper oxide has also been used as catalyst in the synthesis of aryl sulfides from aryl halides with thiourea [Reddy *et al.* (2011)] and in oxidative degradation of methylene blue [Srivastava *et al.* (2011)]. Catalytic activity and sensing property commonly depends on the specific surface area, pore volume, pore size etc. Nanocrystalline copper oxide has different morphologies which depend on the type of preparation methods, such as nanofibers [Wu

et al. (2006)], nanorods [Christy *et al.* (2013)], nanoribbons [Ke *et al.* (2009)], nanoplates [Li *et al.* (2012)], spherical and cubes [Ahmed *et al.* (2011)].

Nanocrystalline copper oxide has been synthesized by several methods such as alcohothermal [Hong *et al.* (2002)] sonochemical [Wongpisutpaisan *et al.* (2011)], electrospinnig [Wu *et al.* (2006)], combustion [Christy *et al.* (2013)], hydrothermal [Liu *et al.* (2012)], solvothermal [Behnoudnia and Dehghani (2013)], solid-state reactions [Díaz *et al.* (2011)], pyrolysis [Chiang *et al.* (2012)], laser ablation [Amikura *et al.* (2008)], microwave irradiation [Katoh *et al.* (2011)], micro-emulsion [Nassar and Husein (2007)], thermal decomposition [Dong *et al.* (2011)] and wire explosion process [Lee *et al.* (2012)]. These methods require sophisticated and expensive apparatus. The main drawbacks of the high temperature process are that the products obtained generally possess low surface area and inhomogeneity. The process homogeneous precipitation method has also been used by some authors [Katoh *et al.* (2011), Xiang *et al.* (2010), Bayal and Jeevanandam (2012a)]. Katoh *et al.* (2011) have reported the synthesis of nanocrystalline copper oxide using 2.45 GHz microwave irradiation, Xiang *et al.* (2010) have reported the preparation of CuO nanoparticles using cetyltrimethylammonium bromide (CTAB) as a surfactant, while Bayal and Jeevanandam (2012a) required long precipitation time (4 hour) for its synthesis. In the present work, pure nanocrystalline copper oxide has been synthesized at low temperature in short precipitation time (1 hour) without using any surfactant or microwave irradiation. The importance of the homogeneous precipitation process on the other methods includes easy control of uniform particle size and also offers simple and low-cost. It is the first new environmental friendly method to synthesize nanocrystalline CuO with dandelion-like morphology using copper acetate and ammonia solution.

4-Nitrophenol (4-NP) and its derivatives are common organic pollutants that occur in industrial waste water. They usually result from the production and utilization of insecticides, synthetic dyes, explosive, pesticides and herbicides [Solanki and Murthy (2011)].

4-Aminophenol (4-AP) is very useful and significant in many applications that include analgesic and antipyretic drugs, photographic developer, corrosion inhibitor in paints, anticorrosion-lubricating agent in fuels, hair-dyeing agent and so on [Zhang *et al.* (2011)]. Because of the above reasons, the conversion of nitrophenol to aminophenol is quite important. Though there are many methods for its conversion [Du *et al.* (2004), Abbar *et al.* (2007), Polat *et al.* (2002)], the method using sodium borohydride as reducing agent in aqueous medium under mild conditions was relatively simple and clean. But the reduction of 4-NP is very slow by using merely the reducing agent sodium borohydride [Kojima *et al.* (2002), Liu *et al.* (2009)]. Therefore, the study for searching efficient catalysts which can catalyze the direct hydrogenation of 4-NP using sodium borohydride becomes more significant from the point of view of pollution abatement. Hence, there is an increasing demand for a better process for the direct catalytic reduction of 4-nitrophenol to 4-aminophenol. This prompted the authors to synthesize an effective and better catalyst than earlier reported work [Bayal and Jeevanandam (2012a)]. For this purpose nanocrystalline CuO has been synthesized and its catalytic property for the reduction of 4-NP to 4-AP has been explored.

3.1.2. Experimental

(i) Materials

Copper acetate (MERCK®), ammonia solution (25%, RANKEM®), 4-nitrophenol (SRL®), $NaBH_4$ (HIMEDIA®) were used as reagents as received without further purification. The solutions were prepared using Millipore® water.

(ii) Synthesis

In the present study, nanocrystalline copper oxide powder was prepared using suitable precursor by homogeneous precipitation method. The details of procedure are as follows. 90 mL aqueous solution of copper acetate (7 mmol) and 12 mL of 25% ammonia solution were taken in a 250 mL beaker. The solution was heated to ~ 80 ^{o}C with continuous stirring for 1 hour. During the reaction, a black precipitate formed, which was filtered off, washed with water many times to remove the impurities and then dried at 80 ^{o}C in an oven. The as-prepared powder was calcined in air at 300 ^{o}C and 400 ^{o}C temperature for 1 hour inside a muffle furnace (Nabertherm®, heating rate = 2 ^{o}C/min). The color of the nanocrystalline copper oxide powder before and after calcination was black.

(iii) Catalytic activity test

The catalytic reactivity of the synthesized nanocrystalline CuO powder was tested for the reduction of 4-nitrophenol to 4-aminophenol using $NaBH_4$ as the reducing agent at room temperature [Bayal and Jeevanandam (2012a)]. This reaction has also been used earlier to examine the catalytic activity of different metal oxide nanoparticles [Bayal and Jeevanandam (2012a), Chiou *et al.* (2013), Chi *et al.* (2012), Mandlimath and Gopal (2011)]. About 50 mL aqueous solution of 4-nitrophenol (3 mmol) and 50 mL of freshly prepared aqueous solution of $NaBH_4$ (0.53 mol / L) were taken in a 250 mL beaker. To the above mixture ~ 8 mg of the catalyst (nanocrystalline CuO powder) was added with constant stirring at room temperature. The decolorization of the mixture indicated the complete reduction of 4-nitrophenol (yellow colored solution) to 4-aminophenol and the time taken for the same was noted.

3.1.3. Results and discussion

Appropriate amount of aqueous ammonia solution was added to aqueous copper acetate solution which yielded soluble Cu $(NH_3)_4^{2+}$ complex ion (blue color) at about 80 ^{o}C.

CuO particles were formed [Srivastava *et al.* (2011), Hu *et al.* (2013)] by the following reactions.

$$Cu(CH_3COO)_2\,(aq.) + 4NH_3\,(aq.) \longrightarrow Cu(NH_3)_4^{2+}\,(aq.) + 2CH_3COO^-\,(aq.) \quad (3.1.1)$$

$$Cu(NH_3)_4^{2+}\,(aq.) \xrightarrow{\triangle} Cu^{2+} + 4NH_3\,(g) \quad (3.1.2)$$

$$Cu^{2+} + [O] \longrightarrow CuO\ (black) \quad (3.1.3)$$

The XRD data confirms the formation of pure CuO.

The powder XRD patterns of as-prepared and calcined CuO samples are shown in Figure 3.1.1. Diffraction peaks of as-prepared and calcined samples were observed at $2\theta \approx 32.6^o$, 35.6^o, 38.6^o, 45.5^o, 48.9^o, 53.5^o, 57.7^o, 61.5^o, 66.2^o, 72.5^o, 74.9^o, and 82.5^o. These peaks are indexed as (110), (11$\bar{1}$), (111), (11$\bar{2}$), (20$\bar{2}$), (020), (202), (11$\bar{3}$), (31$\bar{1}$), (311), (004), and (31$\bar{3}$) diffraction planes of monoclinic phase of CuO with lattice parameters of a = 0.4688 nm, b = 0.3422 nm and c = 0.5132 nm (JCPDS file no. 48-1548). The XRD patterns of as-prepared and calcined samples show peaks of only CuO indicating the absence of any impurity. In the present work, high purity nanocrystalline CuO is obtained by homogeneous precipitation method. The crystallite size of as-prepared and calcined nanocrystalline CuO was calculated using the Debye-Scherrer formula [Cullity and Stock (2001)]. The crystallite size of as-prepared and calcined powder at 300 ^{o}C and 400 ^{o}C are 7.9 nm, 11.2 nm and 14.5 nm respectively.

The thermal gravimetric analysis pattern of the nanocrystalline CuO powder is shown in Figure 3.1.2. The overall weight loss (about 5.6 mass %) between 39-400 ^{o}C is attributed to the physically adsorbed water. The repeatability of mass % of CuO at 39 ^{o}C is 99.92 ± 0.01633 and at 400 ^{o}C is 94.31 ± 0.02582 respectively. There is nearly no weight loss at temperatures above 400 ^{o}C.

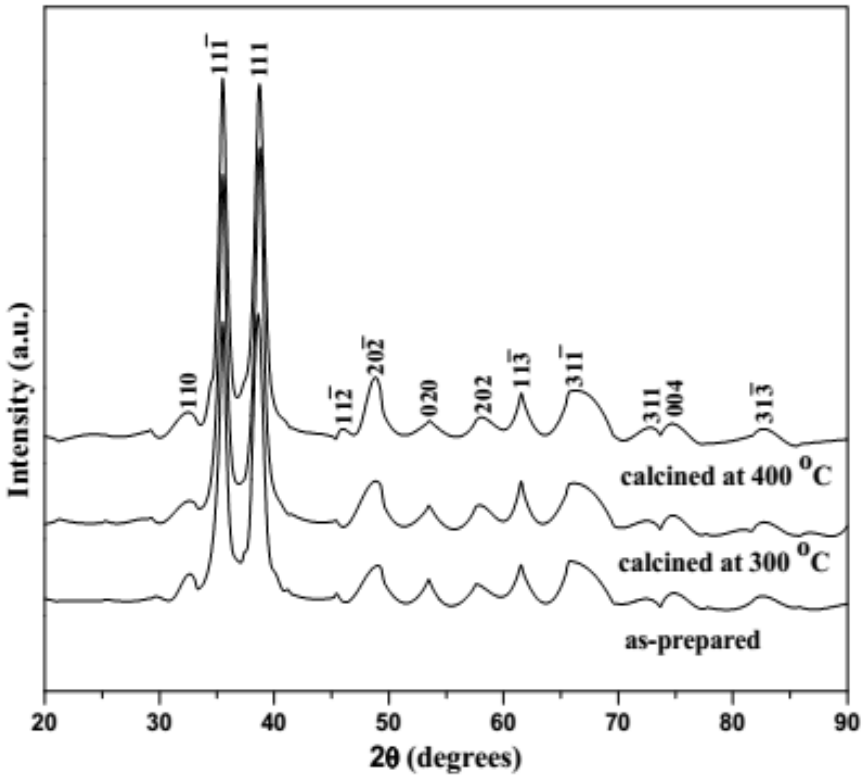

Figure 3.1.1. XRD patterns of nanocrystalline CuO (as-prepared and after calcination).

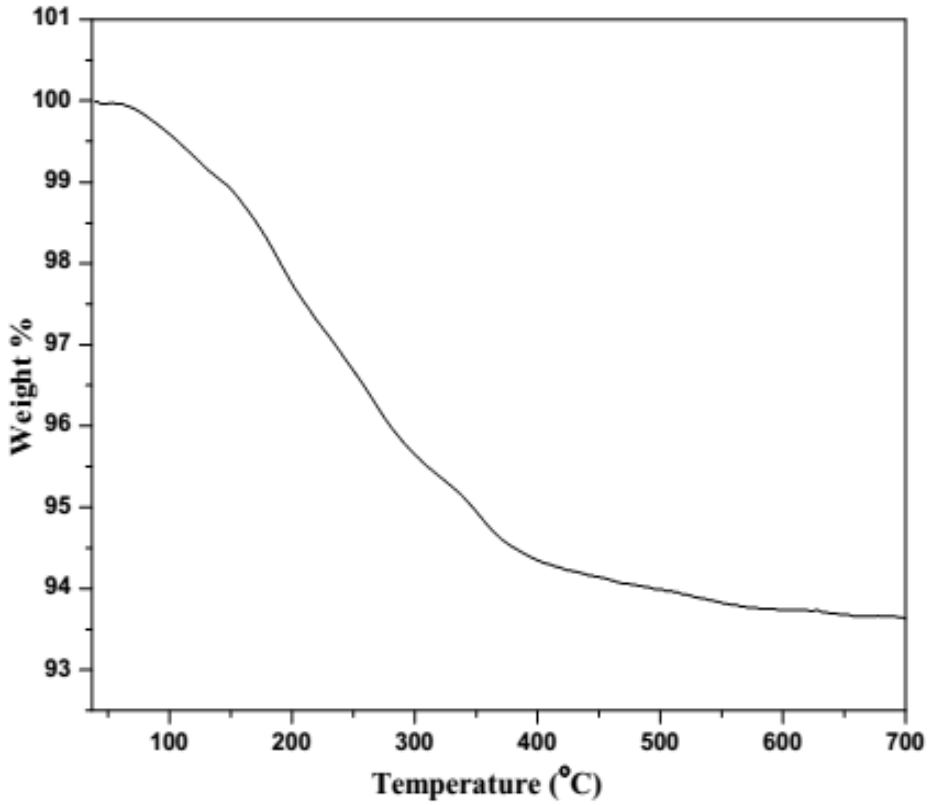

Figure 3.1.2. Thermal gravimetric analysis curve of nanocrystalline CuO.

The FT-IR spectra of as-prepared and calcined CuO samples show broad bands at about 3412 and 3490 cm^{-1} which are attributed to O-H stretching vibrations arising from the moisture present in the KBr used for making the pellets in an open air shown in Figure 3.1.3 [Pendashteh *et al.* (2013)]. The band at about 1648 cm^{-1} present in the spectra of as-prepared and calcined samples at 300 ^{o}C are assigned to the bending vibration of water molecule [Srivastava *et al.* (2011)]. This band disappears in the spectra of the sample calcined at 400 ^{o}C. There are bands between 1547-1346 cm^{-1} resulting from the C=O, carbon-carbon (C-C) and carbon-hydrogen (C-H) vibrations [Behnoudnia and Dehghani (2013)]. δ(OH) exhibits bands between 1000 and 923 cm^{-1} in the spectra [Hosny and Zoromba (2012)]. In nanocrystalline copper oxide powder, Cu-O stretching frequency appears in the range 500-840 cm^{-1} [Srivastava *et al.* (2011)].

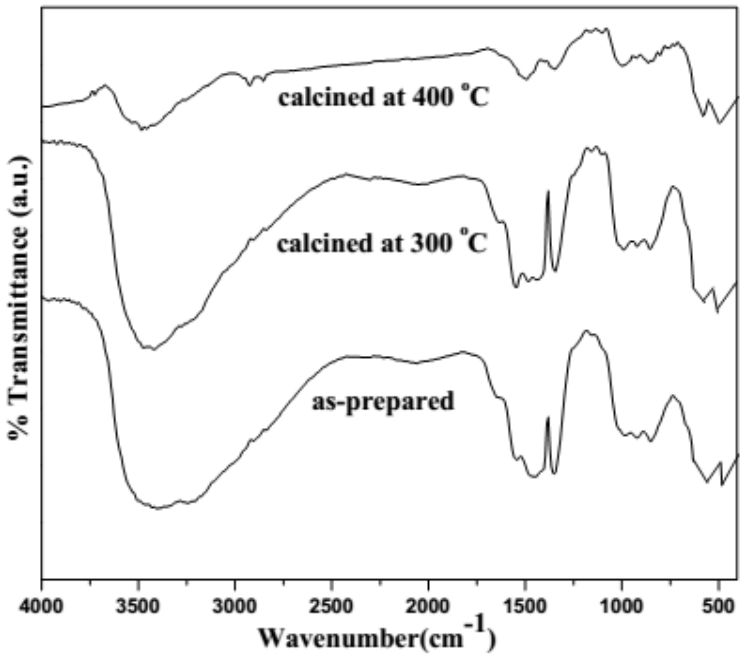

Figure 3.1.3. FT-IR spectra of nanocrystalline CuO (as-prepared and after calcination).

Diffuse reflectance spectra of nanocrystalline CuO powder are shown in Figure 3.1.4. The absorption peak at about 340 nm indicates that the band gap is due to intrinsic transition of CuO nanoparticles [Srivastava *et al.* (2011)].

The reflectance spectra were analyzed by using the Kubelka–Munk function [Kumar *et al.* (2000)]:

$$F(R) = (1-R)^2/2R \qquad (3.1.4)$$

where F(R) is the Kubelka-Munk function which corresponds to the absorbance and R is the reflectance of the sample. The relation between frequency and absorption coefficient of semiconductor is given by:

$$(\alpha h\upsilon)^2 = K(h\upsilon - E_g) \qquad (3.1.5)$$

where α is the absorption coefficient, K is a proportionality constant and υ is the frequency of photons. This equation has been used to calculate the band gap (E_g) of the nanocrystalline CuO powder. The $(\alpha h\upsilon)^2$ versus $h\upsilon$ is plotted in Figure 3.1.4(b) on the basis of data obtained from Figure 3.1.4(a) and the band gap estimated at ~ 1.87 eV corresponds to the reported value of CuO [Srivastava *et al.* (2011), Liu *et al.* (2012), Bayal and Jeevanandam (2012)].

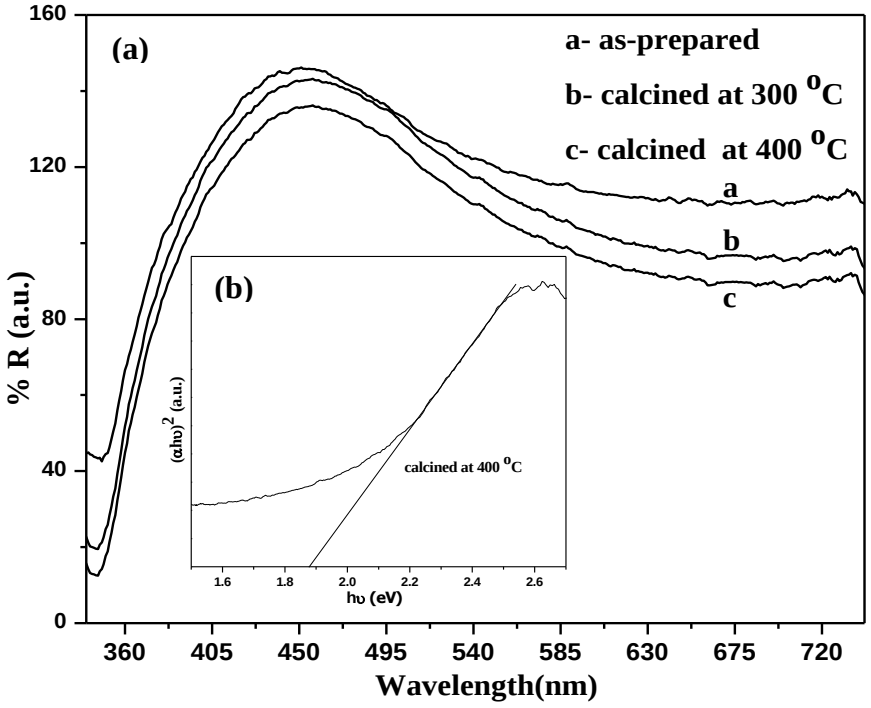

Figure 3.1.4. (a) Diffuse reflectance spectra of nanocrystalline CuO, and (b) The plot of $(\alpha h\upsilon)^2$ vs. $h\upsilon$ according to the data from (a).

Diffuse reflectance spectra confirmed a small size of particles which attributed to the strong quantum confinement of the excitonic transition for nanocrystalline CuO [Nasrabadi *et al.* (2013)].

FE-SEM images of nanocrystalline CuO (before and after calcination) in different magnifications are shown in Figures 3.1.5 and 3.1.6. The FE-SEM image of nanocrystalline CuO before calcination shows agglomeration of spherical particles forming a few solid microspheres with an average diameter of 1.73 ± 0.14 μm (Figures 3.1.5a and 3.1.6a). The nanocrystalline CuO calcined at 300 ^{o}C shows the formation of dandelion-like microspheres (Figures 3.1.5b and 3.1.6b), consisting of small particles. On calcination at 400 ^{o}C, more dandelion-like microspheres are formed with increase in their size (Figures. 3.1.5c and 3.1.6c). The average estimated diameters of dandelion-like microspheres of CuO calcined at 300 ^{o}C and 400 ^{o}C were 2.40 ± 0.16 μm and 3.35 ± 0.22 μm respectively. In as-prepared CuO powder formation of perfect dandelion-like microspheres does not take place. On increasing calcination temperature, small particles aggregate with the formation of perfect dandelion-like microspheres. The EDX analysis indicates the presence of copper and oxygen elements in the nanocrystalline CuO powder (Figure 3.1.5d). On the basis of EDXA data, the atomic ratio of copper to oxygen in as-prepared sample is 0.76 ± 0.034 while for calcined samples at 300 ^{o} and 400 ^{o}C are 0.80 ± 0.042 and 0.95 ± 0.020, respectively (Table 3.1.1). Atomic ratios confirm the presence of high purity CuO after calcination and also weight percent of Cu increases with increase in calcination temperature.

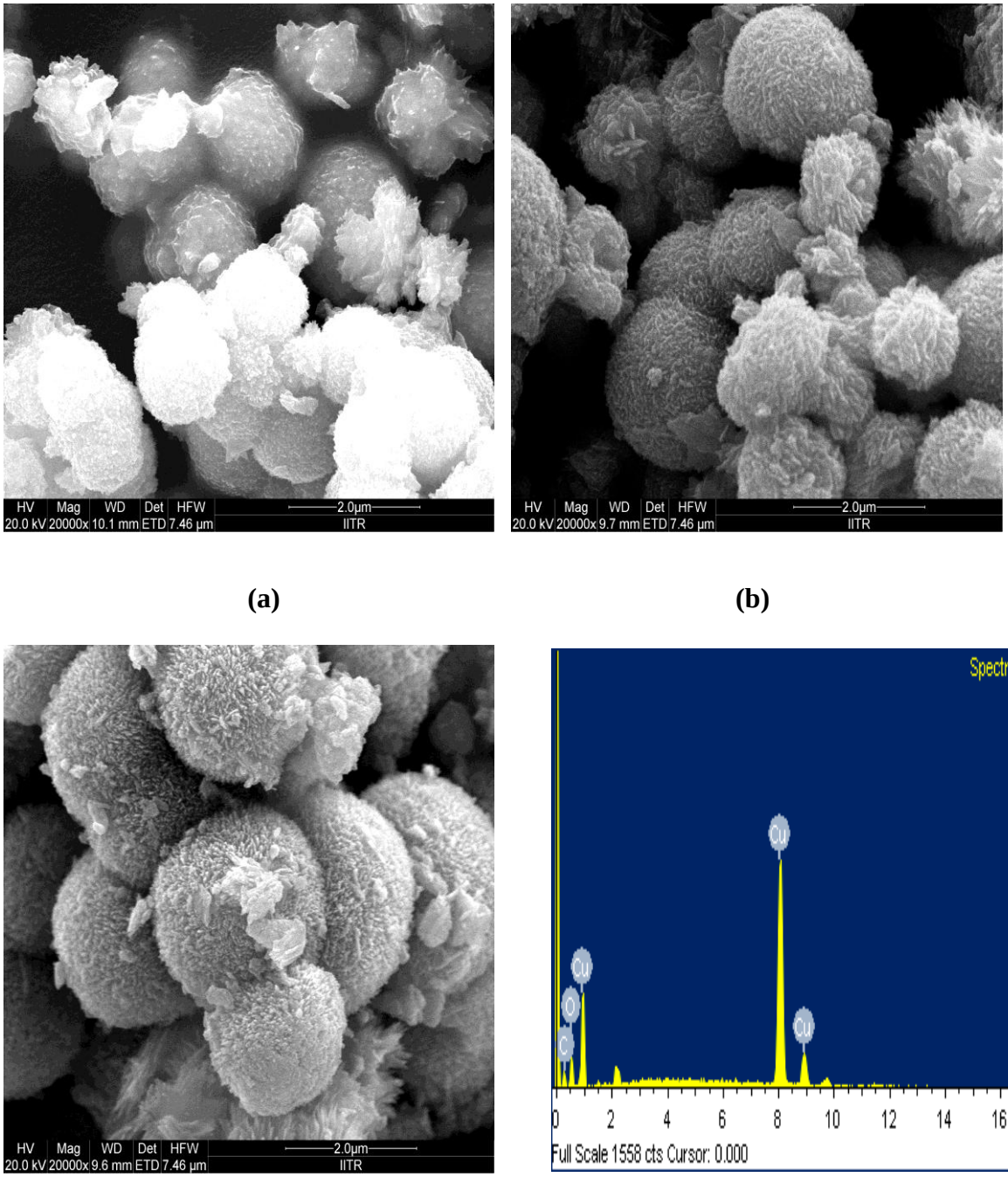

Figure 3.1.5. FE-SEM images of nanocrystalline CuO at low magnification of (a) as-prepared, (b) calcined at 300 ^{o}C, (c) calcined at 400 ^{o}C, and (d) EDX analysis plot of nanocrystalline CuO.

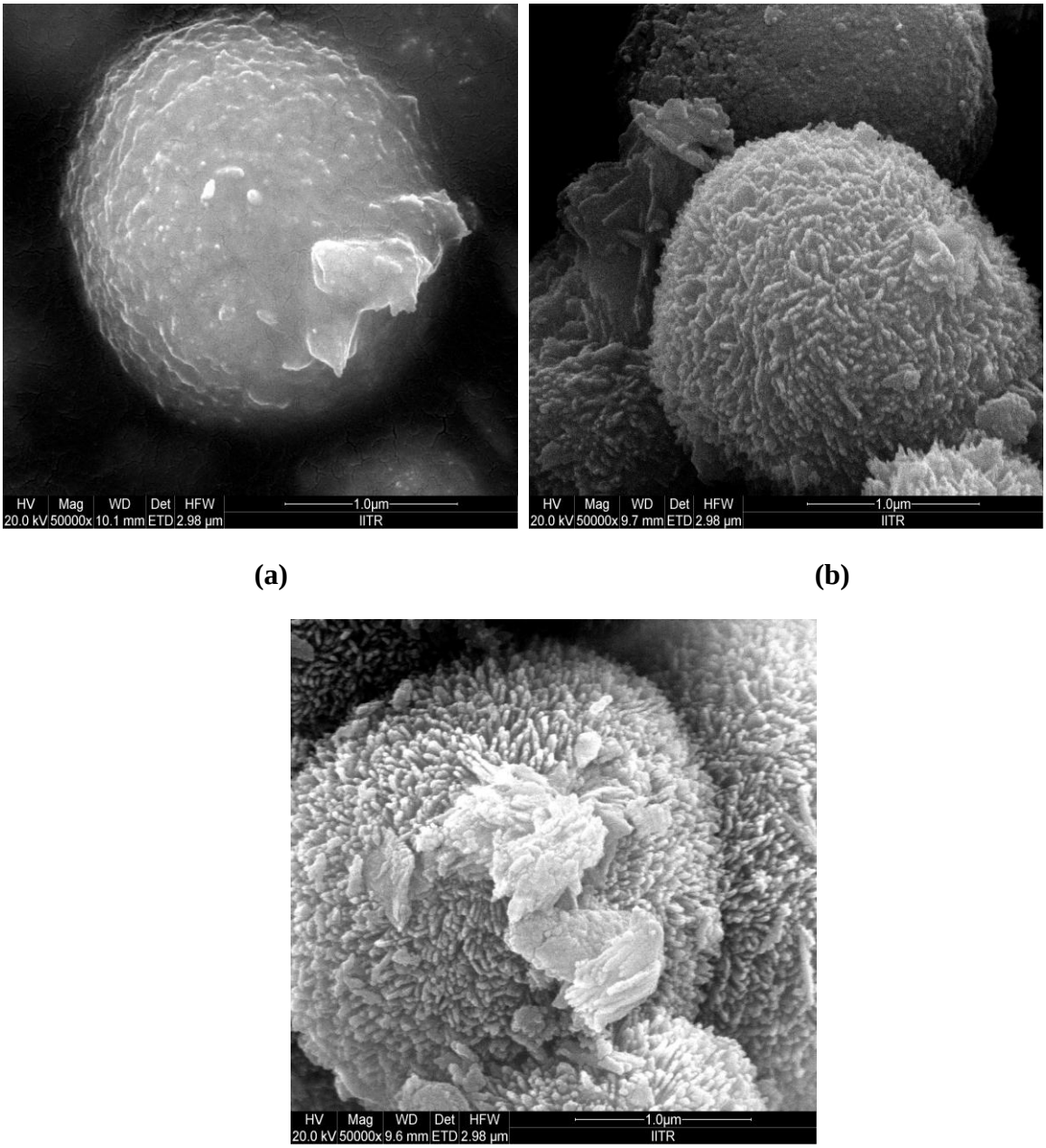

(a) **(b)**

(c)

Figure 3.1.6. FE-SEM images of nanocrystalline CuO at high magnification of (a) as-prepared, (b) calcined at 300 ^{o}C, and (c) calcined at 400 ^{o}C.

Table 3.1.1. EDXA data of as-prepared and calcined nanocrystalline CuO.

Sample	Element	At%	Wt%	Cu/O
Nanocrystalline CuO before calcination	Cu	39.74 ± 1.91	68.93 ± 1.05	0.76 ± 0.034
	O	52.26 ± 0.19	23.06 ± 1.03	
Nanocrystalline CuO calcined at 200 ^{O}C	Cu	41.83 ± 2.22	71.40 ± 1.72	0.80 ± 0.042
	O	52.17 ± 0.15	22.61 ± 1.62	
Nanocrystalline CuO calcined at 400 ^{O}C	Cu	46.78 ± 1.08	75.90 ± 0.86	0.95 ± 0.020
	O	49.22 ± 0.11	20.10 ± 0.61	

Surface area measurements (BET) were carried out for as-prepared and calcined CuO samples. The specific surface area and total pore volume for these samples are given in Table 3.1.2. The results indicate that the as-prepared nanocrystalline CuO powder has high specific surface area (SSA 14.9 ± 0.02 m^2 g^{-1}) and total pore volume (TPV 0.006 ± 0.0002 cm^3 g^{-1}) compared to calcined nanocrystalline CuO powder (300 ^{o}C: SSA 12.3 ± 0.02 m^2 g^{-1}, TPV 0.005 ± 0.0001 cm^3 g^{-1} and 400 ^{o}C: SSA 11.2 ± 0.01 m^2g^{-1}, TPV 0.004 ± 0.0002 cm^3g^{-1}). The specific surface area of nanocrystalline CuO with dandelion-like morphology obtained in the present work is significantly higher than those synthesized through ionic liquid precursor [Li *et al.* (2012)] as nanoplates (10.42 m^2/g) and by hydrothermal method [Hu *et al.* (2013), Yang *et al.* (2011)] as peach kernel-like (5.3 m^2/g), flower-like (5.2 m^2/g), boat-like (5.1 m^2/g) and ellipsoid-like (1.9 m^2/g) morphology.

Table 3.1.2. BET surface area and pore volume of as-prepared and calcined nanocrystalline CuO.

Sample	Surface area ($m^2 g^{-1}$)	Pore volume ($cm^3 g^{-1}$)
CuO (before calcination)	14.9 ± 0.02	0.006 ± 0.0002
CuO (calcined at 300 ^oC)	12.3 ± 0.02	0.005 ± 0.0001
CuO (calcined at 400 ^oC)	11.2 ± 0.01	0.004 ± 0.0002

The catalytic reactivity of the nanocrystalline CuO powder was tested for the reduction of 4-nitrophenol to 4-aminophenol using $NaBH_4$ as reducing agent. The reduction of 4-nitrophenol with sodium borohydride was carried out in the presence as well as in the absence of the catalyst. The decolorization of the test solution in the presence of the catalyst, CuO nanoparticles, indicates complete reduction of 4-nitrophenol. The time required for the reduction is reported in Table 3.1.3. 4-nitrophenol does not get reduced in the absence of the catalyst. The calcined nanocrystalline CuO took 6-8 minutes for reducing the 4-nitrophenol solution. According to the reported mechanism for the reduction of 4-nitrophenol [Solanki and Murthy (2011), Zhang *et al.* (2011), Mandlimath *et al.* (2011)], the adsorption of 4-nitrophenolate and BH_4^- ions take place on the surface of nanocrystalline CuO by chemisorption process (Figure 3.1.7). Then after, nanocrystalline CuO starts the catalytic reaction by relaying electrons from the donor BH_4^- to the NO_2 group (acceptor) to form 4-aminophenolate ions and further desorption of 4-aminophenolate ions occur from the surface of the catalyst. The nanocrystalline CuO acts as a better catalyst for the reduction of 4-nitrophenol (time of reduction: 360 ± 4 - 480 ± 3 s) as compared to the reported results (time of reduction: 960 s) by Bayal and Jeevanandam (2012a).

Table 3.1.3. Time required for the complete reduction of 4-nitrophenol in the presence of nanocrystalline CuO as catalyst.

S.No.	Reaction condition	Time required for the reduction (s)
1.	4-nitrophenol + $NaBH_4$	No reduction
2.	4-nitrophenol + $NaBH_4$ + CuO (as-prepared)	240 ± 6
3.	4-nitrophenol + $NaBH_4$ + CuO (calcined at 300 ^oC)	360 ± 4
4.	4-nitrophenol + $NaBH_4$ + CuO (calcined at 400 ^oC)	480 ± 3

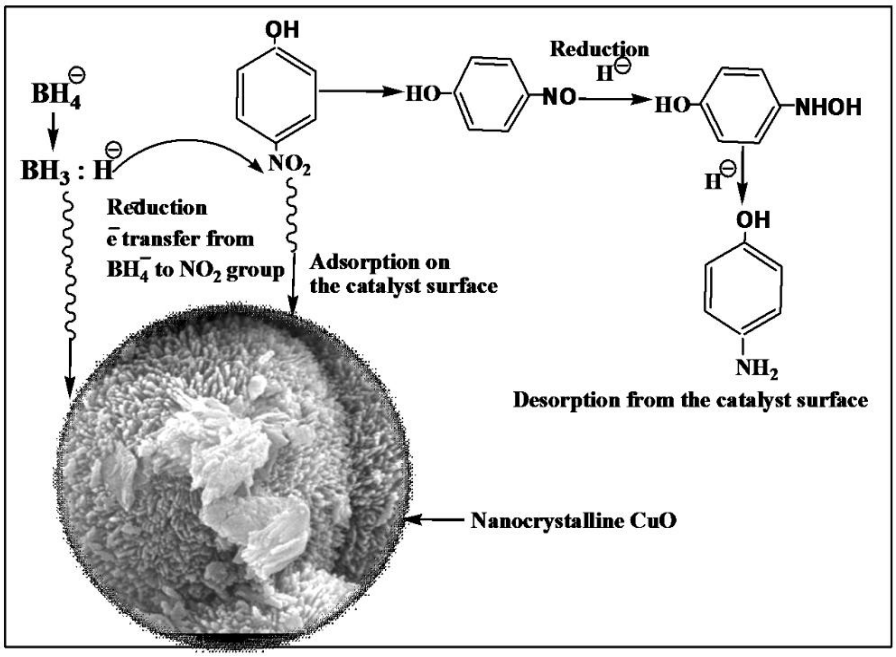

Figure 3.1.7. Schematic diagram indicating the mechanism for the reduction of 4-nitrophenol to 4-aminophenol in the presence of nanocrystalline CuO.

3.2. Zinc oxide nanoparticles (ZnO)

3.2.1. Introduction

Zinc oxide nanoparticles (ZnO-NPs) possess several interesting properties such as optical transparency, electric conductivity, piezoelectricity, non-toxicity, wide availability, low cost and stability [Darezereshki *et al.* (2011), Tari *et al.* (2012)]. They are n-type

semiconductor with a wide band gap (3.3 – 3.6 eV) and large excitation binding energy (60 meV) at room temperature [Darezereshki *et al.* (2011)]. They are used for many applications in various fields including catalysis, gas sensors, solar cells, paints, varnishes, plastics, pharmaceuticals, laser and optoelectronic devices [Hayat *et al.* (2011a), Vafaee and Ghamsari (2007), Zak *et al.* (2011), Ann *et al.* (2014)]. It is usually employed as protective agent in cosmetics and sunscreen products because of its ability to filter UV radiations [Viswanathan and Gupta (2003)]. ZnO-NPs are well known for its antimicrobial and antifungal activity [Kairyte *et al.* (2013), Eskandari *et al.* (2011)]. ZnO powder is an active ingredient for dermatological values in creams, lotions and ointments for its antibacterial properties [El-Diasty *et al.* (2013)]. They have also been used as photocatalysts in degradation of methylene blue due to its high photosensitivity and stability [Shen *et al.* (2008)]. ZnO-NPs have been synthesized using different methods in various morphologies such as fibers [Soofivand *et al.* (2013)], wires [Wang *et al.* (2010)], flowers [Xie *et al.* (2013)], rods [Jia *et al.* (2008)], mallets [Mahmud *et al.* (2006)], tetrapods [Tawale *et al.* (2010)] and rings [Hughes and Wang (2004)] with diverse properties.

ZnO-NPs powder has been synthesized by several methods such as thermal decomposition [Darezereshki *et al.* (2011)], sol–gel [Hayat *et al.* (2011a), Vafaee and Ghamsari (2007)], laser ablation [Thareja and Shukla (2007)], microemulsion [Yildirım and Durucan (2010)], sonochemical [Banerjee *et al.* (2012)], solid state [Pudukudy Yaakob (2014a)], combustion [Tarwal *et al.* (2011)], polymerization [Jajarmi (2009)], vapor deposition [Kouam *et al.* (2008)], spray pyrolysis [Dedova *et al.* (2013)], solvothermal [Tonto *et al.* (2008)] and hydrothermal method [Baruwati *et al.* (2006)]. Homogeneous precipitation method has also been used by some workers to synthesize ZnO-NPs [Ming *et al.* (2012), Liang *et al.* (2011), Samaele *et al.* (2010), Tang *et al.*

(2008), Behnajady *et al.* (2011), Hsieh (2007)]. Ming *et al.* (2012) have reported the synthesis using a Teflon-lined autoclave which required high calcination temperature (450 ^{o}C) while Liang *et al.* (2011) employed a pulse alternative field with a frequency of 50 HZ. Samaele *et al.* (2010), Tang *et al.* (2008) and Behnajady *et al.* (2011) have reported the preparation using sodium dodecyl sulfate (SDS) and oxalic acid as the surfactant and chelating agent respectively. In the present work, ZnO-NPs powder has also been synthesized by homogeneous precipitation method but at low calcination temperature (300 ^{o}C) without using any surfactant, chelating agent, Teflon-lined autoclave or pulse alternative field. The homogeneous precipitation method offers easy control of uniform particle size, environmental-friendly and preparing samples at low temperature in short time in large scale production, not employing any expensive raw materials and complicated equipments. The pathogenic *candida albicans* is the most common microorganism which is responsible for fungal infection [Eskandari *et al.* (2011)]. Its overgrowth causes a variety of infections in the mouth, skin, blood stream and genital regions of both men and women [Molero *et al.* (1998), Berman and Sudbery (2002)]. Recently, fungal infections especially *Candidiasis* has significantly increased and in its treatment only a few antifungal drugs are available. They have developed drug resistance and side effects. Hence, developing of the novel antifungal agents is in urgent demand. This prompted the authors to synthesize ZnO-NPs and to test these for antifungal activity against pathogenic *candida albicans.*

3.2.2. Experimental

(i) Materials

Zinc acetate (MERCK®), ammonia solution (25%, RANKEM®), potato dextrose broth (PDB) medium for fungus cultures (SRL®) were used as received without further purification. For testing antifungal activity *Candida albicans* strain (MTCC 221) was

purchased from the Culture Collection, Chandigarh, India. The solutions were prepared using Millipore® water.

(ii) Synthesis

In the present study, ZnO-NPs powder was prepared using suitable precursor by homogeneous precipitation method. The details of procedure are as follows:

In 250 mL beaker zinc acetate (8 mmol) was dissolved in 90 mL of Millipore water. To this 10 mL ammonium hydroxide (25 % ammonia solution) was added and the contents were heated to ~ 85 ^{o}C with continuous stirring for 2 hour. During the reaction, a milky white precipitate was obtained. It was filtered off, washed with water several times to remove any impurities present and then dried at 70 ^{o}C in an oven for 6 h. The as-prepared powder was calcined in air at 300 ^{o} and 400 ^{o}C at a heating rate of 2 °C/min for 2 h inside a muffle furnace. The color of the ZnO-NPs powder before and after calcination was white.

(iii) Testing of antifungal activity

The antifungal activity of the ZnO-NPs was investigated against *Candida albicans* using the disc-diffusion susceptibility method. 50 mL potato dextrose broth (PDB) medium was prepared by dissolving appropriate amount of potato dextrose powder (39g/L) in Millipore water and mixed it properly. The final volume of 50 mL was made by adding adequate amount of Millipore water to it. Medium was then sterilized at 121 ^{o}C for 15 min. This medium was poured into five different sterilized petri dishes. After solidification of these media, 50 µL suspension cultures of *Candida albicans* was evenly spread on the surface of solidified culture media with sterilized glass spreader. Then sterilized filter paper discs (6 mm diameter) were placed at the centre of each petri dish. The ZnO-NPs were taken at different concentrations of 5, 10, 15 and 20 mg/mL respectively and mixed with sterilized Millipore water using low power sonicator.

Further, each concentration of ZnO-NPs was impregnated onto the discs kept in four petri dishes. In the fifth petri dish the growth of *Candida albicans* was observed for the disc impregnated with only sterile Millipore water in the absence of ZnO-NPs and it was taken as fungal control. Then the dishes were incubated in a thermostatic chamber at 28 ^{o}C for 72 h. All petri dishes were kept in regular observation to examine the zone of inhibition around each disc. The diameters of the clear zone of inhibition were measured in millimetres (mm). To minimize experimental error the experiment was repeated several times.

3.2.3. Results and discussion

Proper amount of aqueous ammonia solution was added to an aqueous zinc acetate solution with continuous stirring for 2 h at ~85 ^{o}C yielding $Zn(OH)_2$ and ZnO (as confirmed by the XRD results). ZnO-NPs were formed by the following reactions:

$$Zn(CH_3COO)_2 \bullet 2H_2O + 2NH_3\ (aq.) \longrightarrow Zn(NH_3)_2(CH_3COO)_2 + 2H_2O \quad (3.2.1)$$

$$Zn(NH_3)_2(CH_3COO)_2 + 2H_2O \longrightarrow Zn(OH)_2 + 2CH_3COONH_4 \quad (3.2.2)$$

$$Zn(OH)_2 \longrightarrow ZnO + H_2O \quad (3.2.3)$$

The XRD data confirm the formation of pure ZnO-NPs after calcination.

The powder XRD patterns of as-prepared and calcined ZnO samples are shown in Figure 3.2.1. In the case of XRD pattern of the as-prepared sample there are two phases, one due to orthorhombic phase of $Zn(OH)_2$ (JCPDS file no. 89-0138) and the second for hexagonal wurtzite phase of ZnO (JCPDS file no. 79-2205). After calcination at 300 ^{o}C and 400 ^{o}C diffraction peaks were observed at $2\theta \approx 31.7^{o}$, 34.3^{o}, 36.3^{o}, 47.5^{o}, 56.5^{o}, 62.8^{o}, 66.3^{o}, 67.9^{o}, 69.0^{o}, 72.6^{o}, and 76.8^{o}. These peaks are indexed as (100), (002), (101), (102), (110), (103), (200), (112), (201), (004), and (202) diffraction lines respectively corresponding to hexagonal ZnO with lattice parameters of a = 0.3250 nm and c = 0.5207 nm (JCPDS file no. 79-2205). These results show that after calcination $Zn(OH)_2$

decomposes and high purity of hexagonal structure of ZnO is formed. The crystallite sizes of as-prepared and calcined ZnO-NPs were calculated by means of an X-ray line-broadening method using the Debye-Scherrer formula [Cullity and Stock (2001)]:

$$D = [0.89 \lambda / \beta \cos \theta] \quad (3.2.4)$$

where D is the crystallite size in nanometers. 0.89 represents a dimensionless constant k, λ is the wavelength of Cu-Kα (0.15406 nm), β is the full width at half maxima (FWHM, radian) of the diffraction peak and θ is the Bragg diffraction angle (degree). The crystallite sizes of as-prepared and calcined ZnO powder at 300 ^{o}C and 400 ^{o}C were found to be 27.6 nm, 29.4 nm and 31.7 nm, respectively.

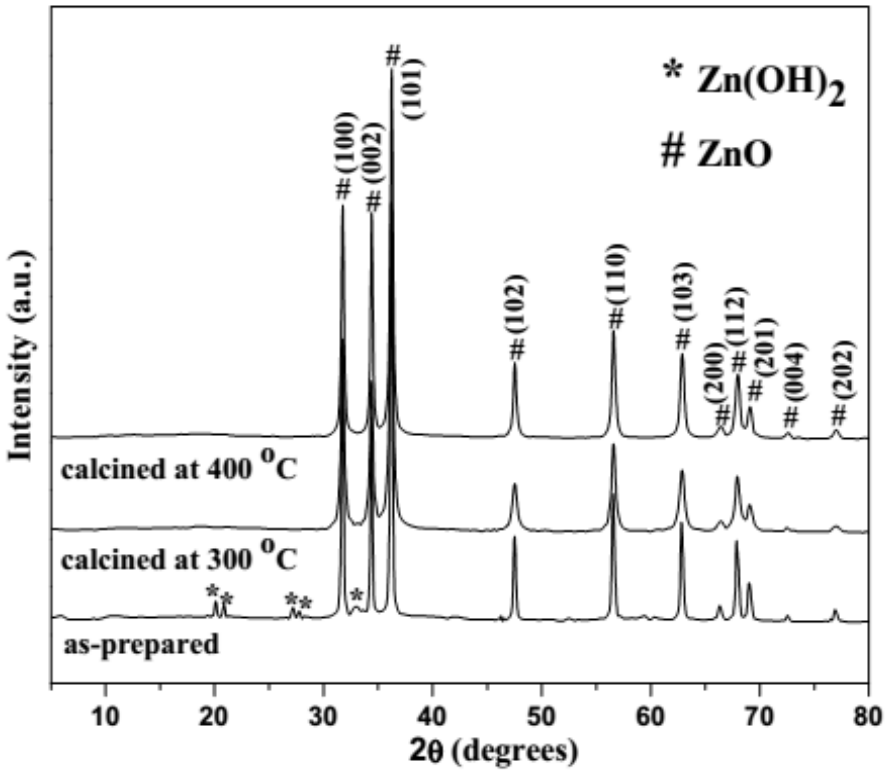

Figure 3.2.1. XRD patterns of as-prepared and calcined samples at 300 ^{o} and 400 ^{o}C.

The thermal gravimetric analysis patterns for as-prepared powder show weight loss of about 18 % which is mainly attributed to the release of water molecules from the decomposition of anhydrous $Zn(OH)_2$ to ZnO (Figure 3.2.2). There is no weight loss after 300 ^{o}C, confirming the formation of pure ZnO.

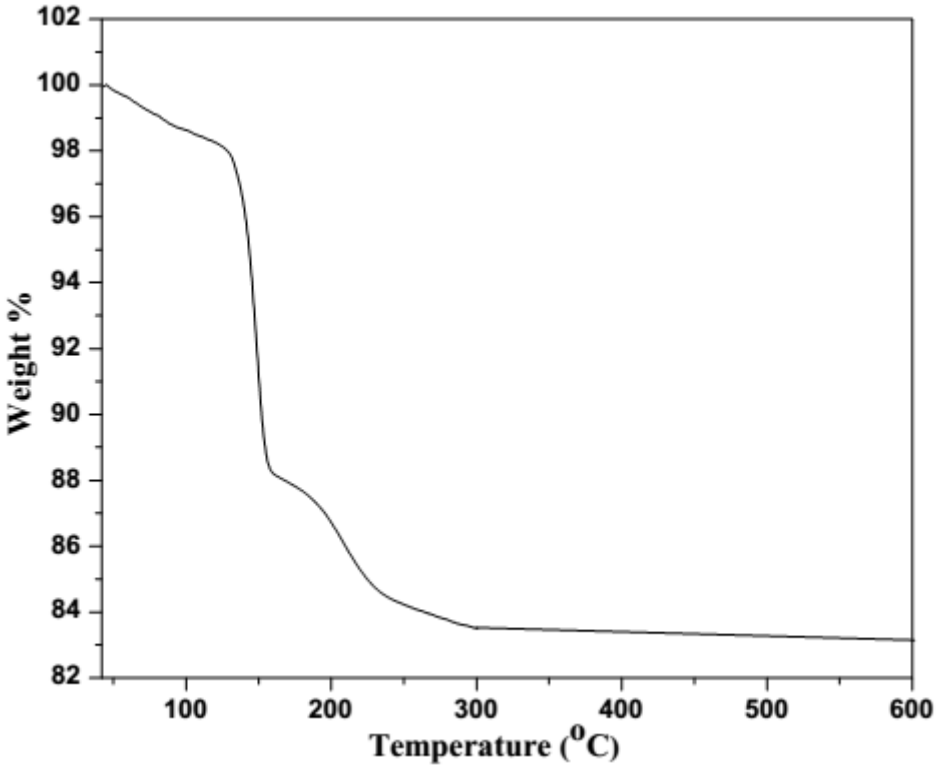

Figure 3.2.2. Thermal gravimetric analysis curves of as-prepared sample.

The FT-IR spectra of as-prepared and calcined samples are shown in Figure 3.2.3. The broad band observed in the 3346 cm^{-1} region corresponds to the stretching vibration of O–H bonds due to the adsorbed water molecules in the spectra of as-prepared and calcined samples [Thangaraj *et al.* (2011)]. As the calcination temperature increases this band becomes weaker. The bands at 1544 and 1382 cm^{-1} peaks are attributed to the asymmetric and symmetric C=O bond vibrations respectively in the spectra of as-prepared and calcined (300 ^{o}C) samples [Vafaee and Ghamsari (2007), Abbad *et al.* (2013)]. These bands almost disappear in the calcined sample at 400 ^{o}C. The band at 668 cm^{-1} is ascribed to the presence of hydroxyl group in the as-prepared sample [Thangaraj *et al.* (2011)]. The bands appearing in the range of 546-458 cm^{-1} are attributed to the Zn-O stretching vibrations [Abbad *et al.* (2013), Ansari *et al.* (2011)]. After calcination the complete transformation of hydroxide to the oxide phase takes place.

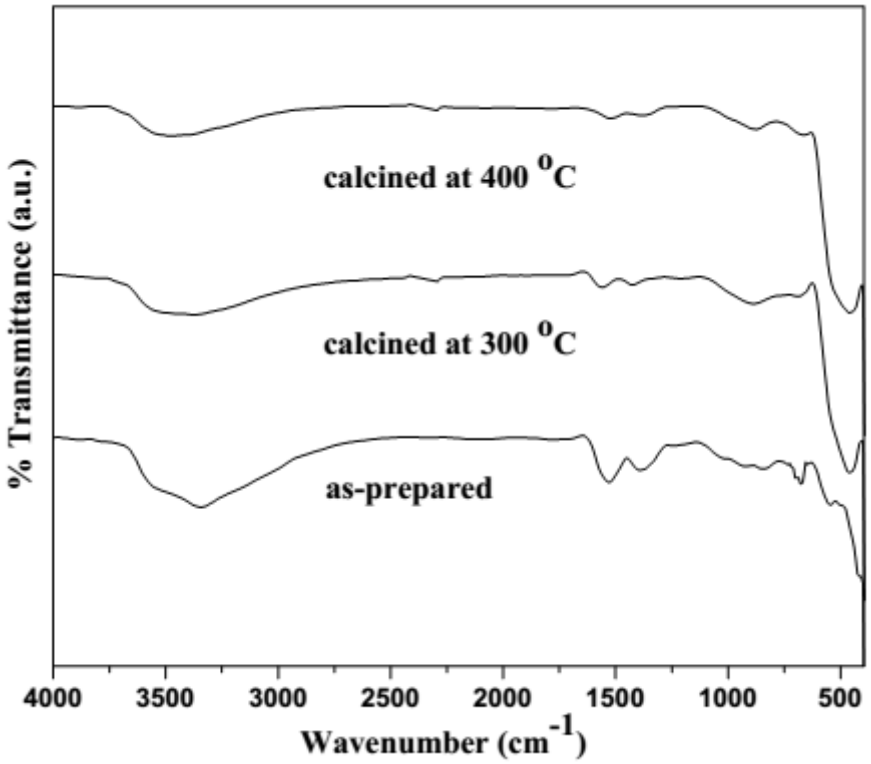

Figure 3.2.3. FT-IR spectra of as-prepared and calcined samples at 300 ^{o} and 400 ^{o}C.

Diffuse reflectance spectra of ZnO-NPs powder calcined at 300 ^{o}C and 400 ^{o}C are shown in Figure 3.2.4(a). The characteristic absorption band at about 385 nm in the UV-visible spectra of calcined samples is attributed to the intrinsic band-gap absorption of ZnO-NPs owing to the electron transitions from the valence band to the conduction band ($O_{2p} \rightarrow Zn_{3d}$) [Zak *et al.* (2011)]. The optical band gap (E_g) of ZnO-NPs is determined by extrapolation of the linear relationship between $(\alpha h\upsilon)^2$ and $(h\upsilon)$ [Yakuphanoglu (2010)]. The $(\alpha h\upsilon)^2$ on the y axis versus photo energy $(h\upsilon)$ on the x-axis is plotted in Figure 3.2.4(b) on the basis of data obtained from Figure 3.2.4(a). The estimated band-gap energy, thus obtained, is ~ 3.22 eV for ZnO-NPs. The band gap is influenced by various factors of the nanoparticles such as morphology, particle size, compositions and the presence of defects (oxygen vacancies) [Zak *et al.* (2011)].

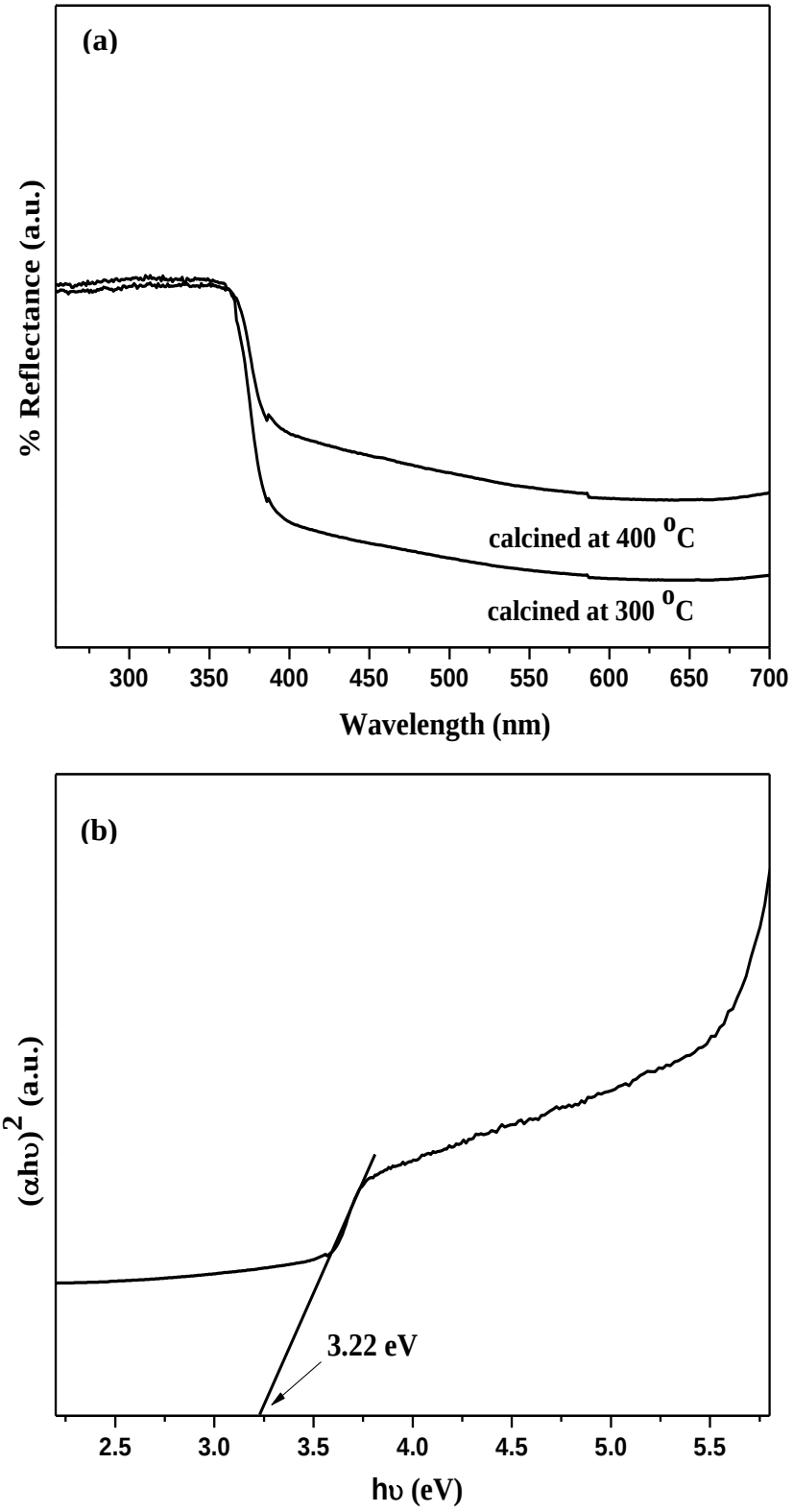

Figure 3.2.4. (a) Diffuse reflectance spectra of ZnO-NPs, and (b) The plot of $(\alpha h\upsilon)^2$ vs. hυ according to the data from (a).

Surface area measurements (BET) were carried out for the as-prepared and calcined samples and the results are represented in Table 3.2.1. It is observed that the as-prepared sample has high specific surface area (SSA ~ 24.6 m^2g^{-1}) and total pore volume (TPV ~ 0.017 cm^3 g^{-1}) as compared to that of the calcined ZnO-NPs (300 ^{o} C: SSA ~ 21.4 m^2g^{-1}, TPV ~ 0.015 cm^3 g^{-1} and 400 ^{o}C: SSA ~ 19.3 m^2g^{-1}, TPV~ 0.013 cm^3 g^{-1}). The specific surface area of ZnO-NPs prepared by other methods like the sonochemical [Banerjee *et al.* (2012)] and wet chemical methods [Bagabas *et al.* (2013)] are about 16.5 m^2g^{-1} and 12.4 m^2g^{-1} respectively which are significantly lower than that obtained in the present method.

Table 3.2.1. BET surface area and pore volume of the samples before and after calcination.

Sample	Surface area (m^2 g^{-1})	Pore volume (cm^3 g^{-1})
As-prepared powder	24.6 ± 0.08	0.017
ZnO-NPs(calcined at 300 ^{o}C)	21.4 ± 0.14	0.015
ZnO-NPs (calcined at 400 ^{o}C)	19.3 ± 0.16	0.013

FE-SEM images of the samples before and after calcination in different magnifications are shown in Figures 3.2.5 and 3.2.6. The FE-SEM images of the sample before calcination show rod-like morphology (Figures 3.2.5(a) and 3.2.6(a)). The calcined (at 300 ^{o}C) ZnO-NPs powder exhibits the agglomerated spherical particles and few rod-like structures (Figures 3.2.5(b) and 3.2.6(b)). From Figures 3.2.5(c) and 3.2.6(c), it is observed that on calcination at 400 ^{o}C the rod-like morphology of ZnO-NPs completely disappeared and only the formation of highly agglomerated spherical particles took place. The EDXA spectrum indicates the presence of only zinc and oxygen elements in the synthesized ZnO-NPs powder, as shown in Figure 3.2.5(d).

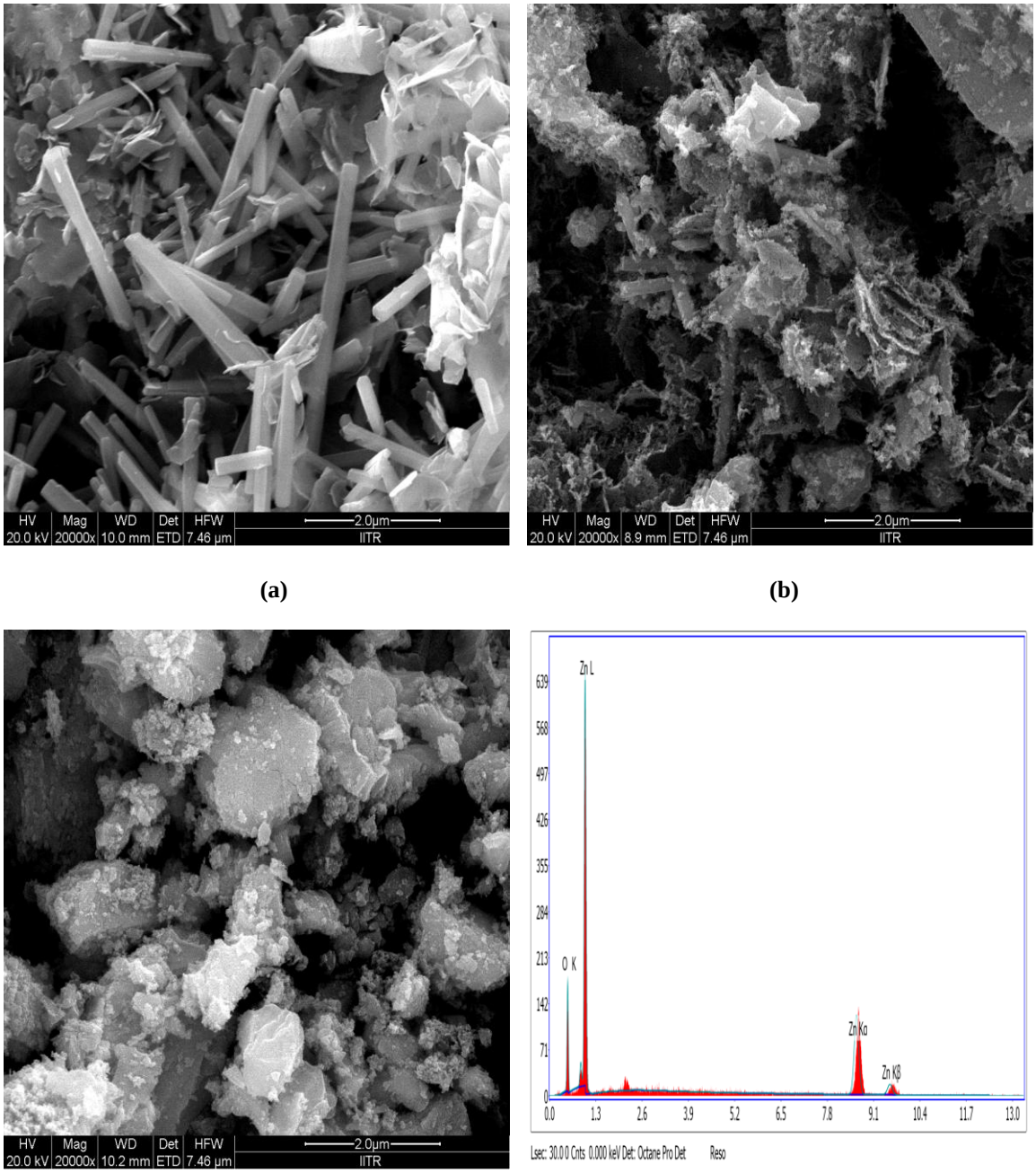

(a) **(b)**

(c) **(d)**

Figure 3.2.5. FE-SEM images of samples at low magnification of (a) as-prepared, (b) calcined at 300 ^{o}C, (c) calcined at 400 ^{o}C, and (d) EDX analysis plot of ZnO-NPs.

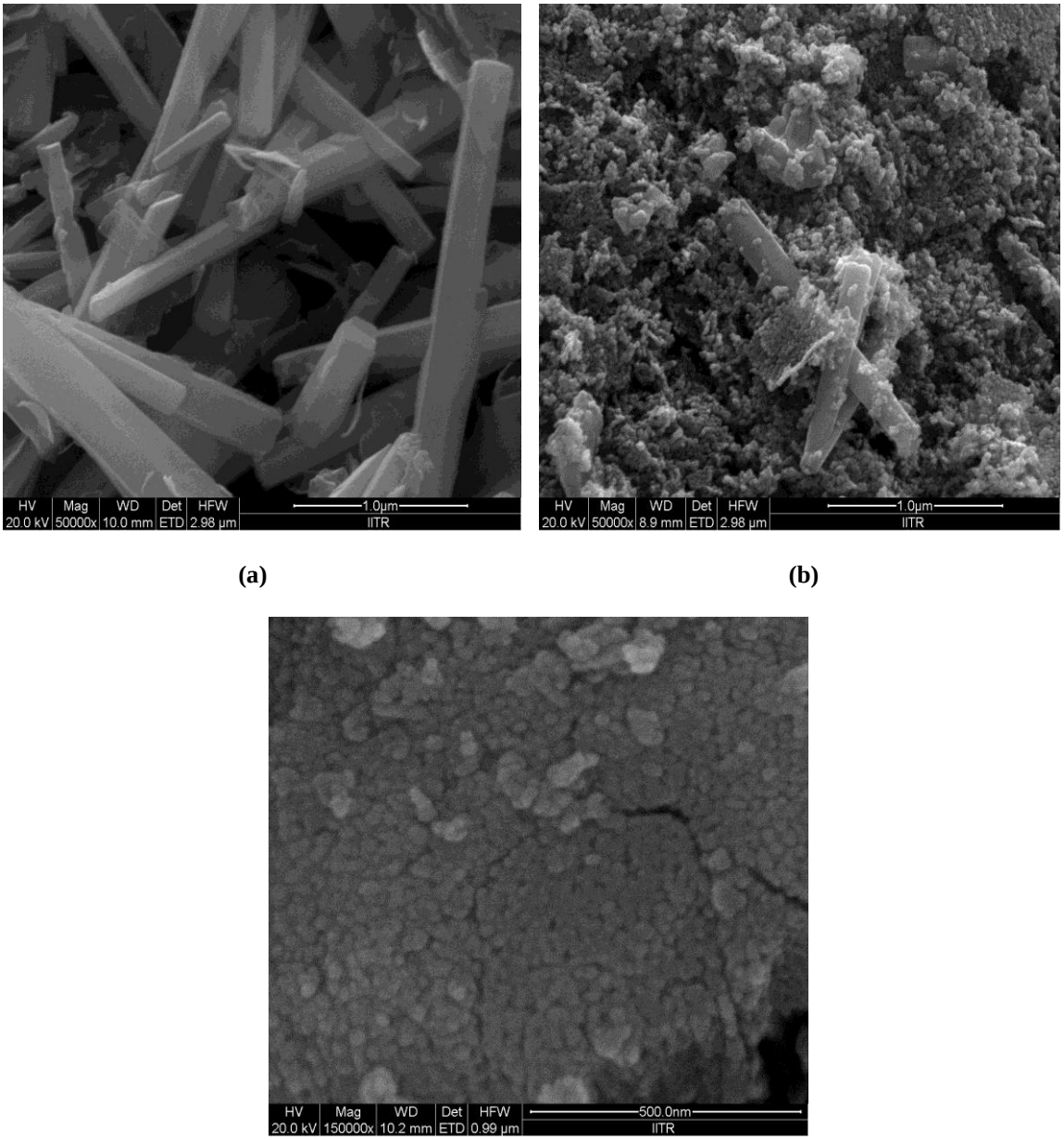

(a) **(b)**

(c)

Figure 3.2.6. FE-SEM images of samples at high magnification of (a) as-prepared, (b) calcined at 300 ^{o}C, and (c) calcined at 400 ^{o}C.

The elemental analysis data of the samples show that the atomic ratio of zinc to oxygen in the as-prepared sample is 0.65 while in the calcined samples at 300 ^{o}C and 400 ^{o}C they are 0.89 and 0.95, respectively (Table 3.2.2). The EDX analysis results confirm the presence of high purity of ZnO-NPs after calcination and this is in good agreement with the XRD results (Figure 3.2.1).

Table 3.2.2. EDXA data of the samples before and after calcination.

Sample	Element	At%	Wt%	Zn/O
As-prepared powder	Zn	39.44	72.68	0.65
	O	60.56	27.32	
ZnO-NPs calcined at 300 ^{O}C	Zn	47.11	78.46	0.89
	O	52.89	21.54	
ZnO-NPs calcined at 400 ^{O}C	Zn	48.72	79.53	0.95
	O	51.28	20.47	

Typical TEM images for calcined ZnO-NPs at 300 ^{o}C and 400 ^{o}C are reported in Figures 3.2.7(a) and 3.2.7(b). It was noticed that the ZnO-NPs obtained on calcination at 300 °C exhibited both spherical and slightly distorted triangular morphology. On the other hand, the nanoparticles calcined at 400 °C have a fairly uniform distribution of hexagonal shape. The number of hexagonal shaped ZnO-NPs increases with rise of the calcination temperature. The average particle size calculated for calcined ZnO-NPs at 300 ^{o}C and 400 ^{o}C from the TEM images are 30.6 ± 0.3 nm and 33. 8 ± 0.5 nm, respectively.

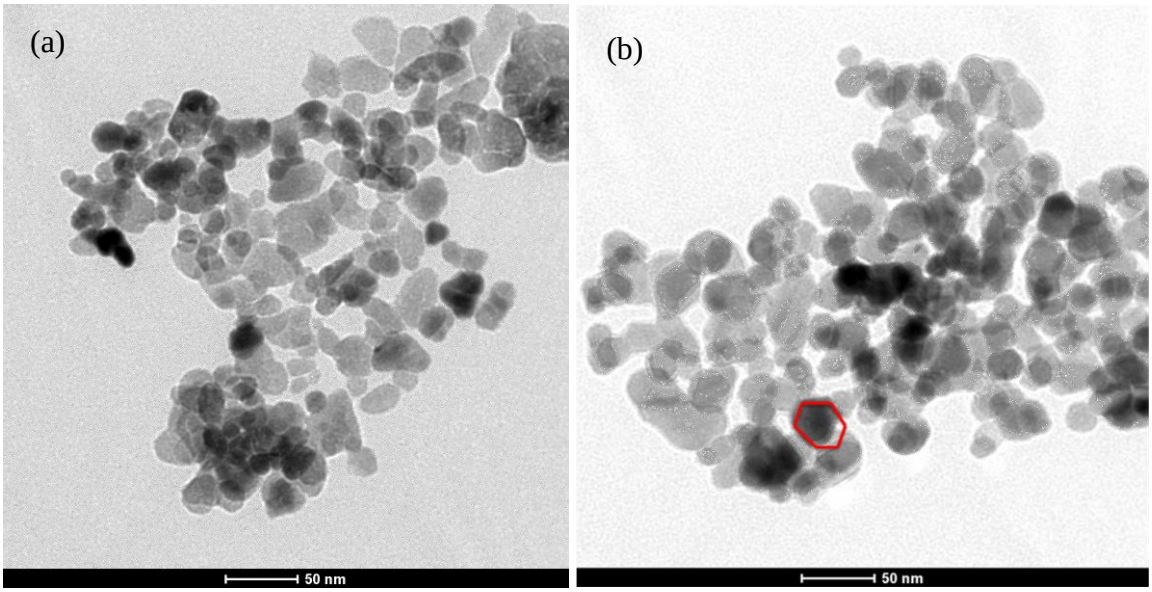

Figure 3.2.7. TEM images of ZnO-NPs (a) calcined at 300 ^{o}C and (b) 400 ^{o}C.

The antifungal activity of ZnO-NPs was tested against pathogenic *Candida albicans* by disc diffusion susceptibility method (Figure 3.2.8). The diameter of inhibition zones around each disc in the presence of different concentrations of ZnO-NPs (5, 10, 15 and 20 mg/mL) is represented in Table 3.2.3. No inhibition zone was observed around the disc in the absence of ZnO-NPs (Figure 3.2.8(a)). The antifungal activity is observed to be dependent on the concentration of ZnO-NPs (Figures 3.2.8(b)–(e)). The inhibition areas increases with respect to the concentration of ZnO-NPs in every instance (Table 3.2.3). The Table 3.2.3 shows that the minimum zone of inhibition (1.5 ± 0.1 mm) is obtained for 5 mg/mL and the largest zone of inhibition (11.4 ± 0.2 mm) is found for 20 mg/mL ZnO-NPs concentration. The mechanism of antifungal activity of ZnO-NPs is explained [Eskandari *et al.* (2011), Rasmussen *et al.* (2010), Shoeb *et al.* (2013), Gondal *et al.* (2012)] on the basis of production of reactive oxygen species (ROS) such as hydrogen peroxide, superoxide anion, hydroxyl radical, and hydroxyl ion. The generation of ROS from ZnO-NPs is related to their semiconductor properties. There are large numbers of valence band holes and/or conduction band electrons in ZnO-NPs which serve its purpose in redox reactions even in the absence of UV light. ZnO-NPs are very small in size so that the nanocrystal quality decreases and thus the interstitial zinc ions, oxygen vacancies and also possibly donor/acceptor impurities increase. These crystal defects lead to a large number of electron-hole pairs ($e^- + h^+$). Holes being powerful oxidants split water molecules derived from the ZnO aqueous environment into H^+ and OH^-. The conduction band electrons, which are good reducers, move to the particle surface and react with dissolved oxygen molecules to generate superoxide radical anions ($O_2^{\bullet -}$). This $O_2^{\bullet -}$ radical anions react with H^+ to generate ($HO_2^{\bullet}$) radicals. These $HO_2^{\bullet}$ molecules further react with electrons producing hydrogen peroxide anions (HO_2^-). These HO_2^- anions further react with hydrogen ions with the formation of hydrogen peroxide (H_2O_2).

The ROS produced in these ways help to rupture fungal cell membrane resulting in possible decrease in fungal enzymatic activity. The generated H_2O_2 can penetrate the cell membrane and kill the fungi. The hydroxyl radicals and superoxides being negatively charged particles remain on the outer surface of the membrane. It has been observed that with the increase in concentration of ZnO-NPs, the generation of H_2O_2 also increases (Table 3.2.3). It is supported from the fact that on increasing the concentration of ZnO-NPs, the fungal activity also increases.

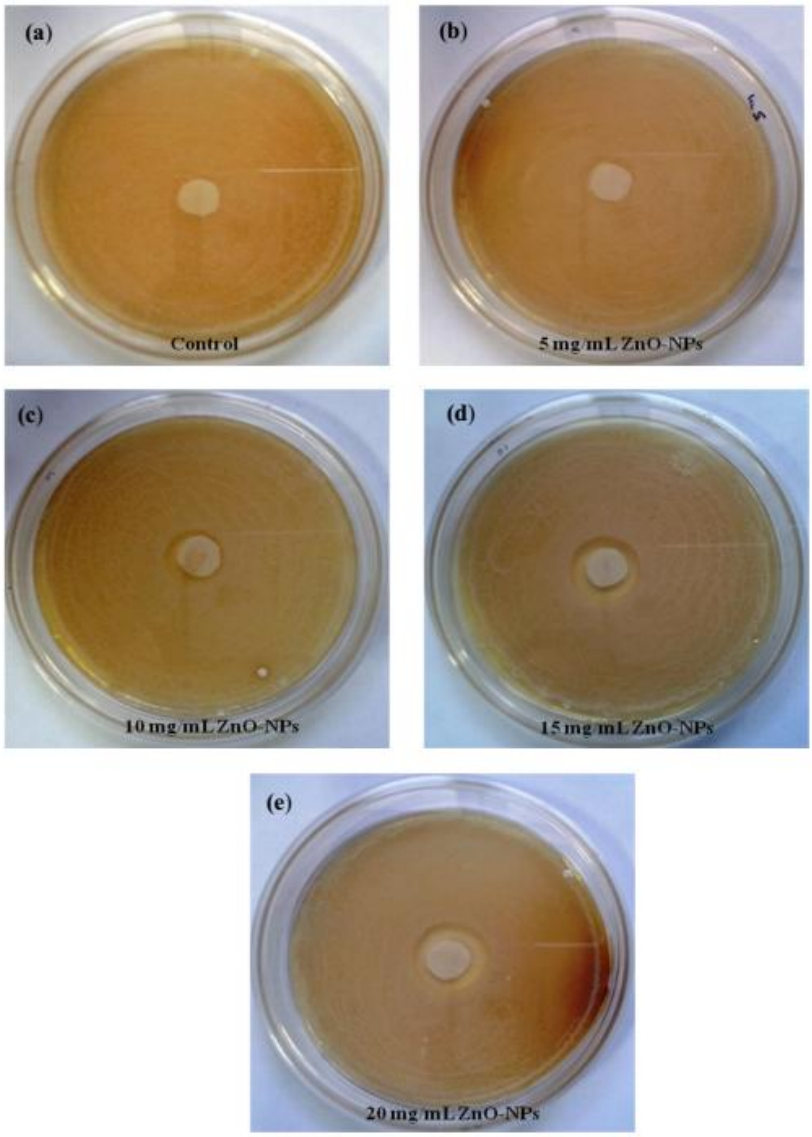

Figure 3.2.8. Antifungal activity of different concentration of ZnO nanoparticles against tested Candida albicans (a) control, (b) 5mg/mL, (c) 10mg/mL, (d) 15mg/mL, and (e) 20mg/mL.

Table 3.2.3. Zones of inhibition observed for different concentration of ZnO-NPs against *Candida albicans* during disc diffusion testing.

Concentration of ZnO-NPs (mg/mL)	**Diameter of the clear inhibition zone (mm)**
Control (Millipore water)	No inhibition zone
5	1.5 ± 0.1
10	5.3 ± 0.2
15	8.6 ± 0.4
20	11.4 ± 0.2

3.3. Nickel oxide nanoparticles (NiO)

3.3.1. Introduction

Nano-sized materials have been widely used in different fields because of their unique physical and chemical properties that are completely changed from those of their bulk counterparts. These properties are extensively affected by the morphology, size, shape and crystalline nature of nanomaterials [Tao *et al.* (2012), Saghatforoush *et al.* (2012), Al-Sehemi *et al.* (2014)]. Among transition metal oxides, NiO nanoparticles are important p-type semiconductor with a stable wide band gap (3.6–4.0 eV) [Kalam *et al.* (2013)]. They have potential applications in gas sensors [Du *et al.* (2012)], magnetic materials [Thota and Kumar (2007)], solar cells [Awais *et al.* (2011)], ceramic materials [Dharmaraj *et al.* (2006)], antioxidant [Saikia *et al.* (2010)], supercapacitors [Yuan *et al.* (2013)], anodes for lithium ion batteries [Cheng *et al.* (2014), Rai *et al.* (2013)] and catalysis [Gallon *et al.* (2011)] due to their high chemical and thermal stability. They have also been used as adsorbent for the removal of most toxic Cr (VI) from aqueous solutions [Behnajady and Bimeghdar (2014)] and malachite green and acid red in pollutants from waste water [Wei *et al.* (2014)]. In addition NiO nanoparticles exhibit antibacterial

activity against *Escherichia coli*, *Bacillus subtilis*, and *Streptococcus aureus* [Baek and An (2011), Pang *et al.* (2009)]. They are too used as good photocatalysts in the degradation of phenol [Hayat *et al.* (2011b)].

NiO nanoparticles have been synthesized by different methods such as solvothermal [Kalam *et al.* (2013)], microemulsion [Du *et al.* (2012)], microwave plasma [Awais *et al.* (2011)], hydrothermal [Wei *et al.* (2014)], sol-gel [Hayat *et al.* (2011)], ultrasonic [Sun *et al.* (2014)], solid state [Niasari *et al.* (2009b)], combustion [Christy and Umadevi (2013)], mechanochemical [Dodd (2009)], thermal decomposition [Hosny (2011)], reverse-micellar [Ahmad *et al.* (2006)], electrospinnig [Guan *et al.* (2003)], vapor deposition [Moravec *et al.* (2011)] and spray pyrolysis method [Wang *et al.* (2004)]. The various preparation methods yield diverse morphologies of NiO nanoparticles such as nanoflakes [Wei *et al.* (2014)], nanotubes [Pang *et al.* (2009)], nanospheres [Dam and Lee (2013)], nanosheets [Tong *et al.* (2013)], nanofibers [Zhang *et al.* (2012)], nanoplatelets [Zheng *et al.* (2009)], nanodisks [Ren *et al.* (2012)], nanorods and nanocubes [Bai *et al.* (2013)]. But, the reported experimental techniques are still limited in laboratory scale due to some insurmountable problems and also need special conditions, tedious procedures, complex apparatus, low-yield and high-cost. The most important disadvantages of the high temperature process are that the products obtained generally possess, low surface area, inhomogeneity and agglomerated particles. The homogeneous precipitation route has been used by a few authors [Rai *et al.* (2013), Karthik *et al.* (2011), Bayal and Jeevanandam (2012a)]. Rai *et al.* (2013) used microwave irradiation for its synthesis which required high calcination temperature (600 ^{o}C for 3 h), Karthik *et al.* (2011) employed polyethylene glycol as a surfactant, while Bayal and Jeevanandam (2012a) required long precipitation time (6 hour) for its synthesis. The present authors utilized homogeneous precipitation method at low calcination temperature (350 ^{o}C for 2h)

without using any surfactant, chelating agent, gelating agent and microwave irradiation. The homogeneous precipitation method has an easy control of uniform particle size and is environmental-friendly in preparing samples at low temperature in short time in large batch production. The calcination temperature was varied to investigate its effect on the morphology, crystallinity, specific surface area, total pore volume and optical band gap of the synthesized samples. In the present work a catalyst has been investigated for the reduction of 4-nitrophenol to 4-aminophenol using sodium borohydride as reducing agent in aqueous medium at room temperature which is comparatively simple, efficient and greener process. The synthesized samples have been characterized and its catalytic activity has been tested for the reduction of 4-NP to 4-AP using $NaBH_4$.

3.3.2. Experimental

(i) Materials

Nickel (II) acetate ($Ni(CH_3COO)_2 \cdot 4H_2O$) (98%, ALDRICH®), ammonia solution (25%, RANKEM®), 4-nitrophenol (SRL®) and $NaBH_4$ (HIMEDIA®) were used as reagents as received without further purification. All solutions were prepared in Millipore® water.

(ii) Synthesis

In this study nanocrystalline NiO powder was prepared using proper precursor by homogeneous precipitation method. The details of procedure are as follows:

About 1.24 g nickel acetate tetrahydrate was dissolved in 80 mL of Millipore water in a 250 mL beaker. To this solution 13 mL ammonium hydroxide (25 % ammonia solution) was added and a blue solution formed. The contents were heated to ~ 78 ^oC with continuous stirring for 1.5 hour. During the reaction, blue color of the solution disappeared and green precipitate was obtained. It was filtered off, washed with water several times to remove any impurities including ammonium acetate and then dried at 80 ^oC in an oven for a few hours. The as-prepared powder was grounded and calcined in air

at 350 and 500 ^{o}C at a heating rate of 1 °C/min for 2 h inside a muffle furnace (Nabertherm). The colors of the as-prepared and calcined samples were green and grey respectively.

(iii) Catalytic reactivity test

The catalytic ability of the synthesized samples was tested for the reduction of 4-nitrophenol to 4-aminophenol using $NaBH_4$ as reducing agent at room temperature [43]. This reaction has also been used in literature to examine the catalytic activity of different metal oxide nanoparticles [Bayal and Jeevanandam (2012a), Chi *et al.* (2012), Mandlimath *et al.* (2011), Solanki and Murthy (2011)]. About 50 mL aqueous solution of 4-nitrophenol (2 mmol) and 50 mL of freshly prepared aqueous solution of $NaBH_4$ (0.53 mol / L) were taken in a 250 mL beaker. To the above mixture about 9 mg of the catalyst (synthesized samples) was added with constant stirring at room temperature. The decolorization of the mixture indicated the complete reduction of 4-nitrophenol (yellow colored solution) to 4-aminophenol (colorless) and the time taken for the same was noted.

3.3.3. Results and discussion

Appropriate amount of aqueous ammonia solution was added to an aqueous nickel acetate solution with continuous stirring for 1.5 h at ~ 78 ^{o}C which yielded green $Ni(OH)_2$ (as confirmed by the XRD results). During the synthesis of nanocrystalline NiO, the following reactions take place:

$$Ni(CH_3COO)_2 \bullet 4H_2O + 4NH_3\,(aq.) \rightarrow Ni(NH_3)_4(CH_3COO)_2 + 4H_2O \quad (3.3.1)$$

$$Ni(NH_3)_4(CH_3COO)_2 + 2H_2O \rightarrow Ni(OH)_2 + 2CH_3COONH_4 + 2NH_3 \quad (3.3.2)$$

In calcination process:

$$Ni(OH)_2 \rightarrow NiO + H_2O \quad (3.3.3)$$

The XRD data confirm the formation of pure nanocrystalline NiO after calcination.

The powder XRD patterns of as-prepared and calcined samples are shown in Figure 3.3.1. XRD pattern of the as-prepared sample show peaks only due to the hexagonal phase of $Ni(OH)_2$ (space group: *P$\bar{3}$m1*, JCPDS file no. 14-0117). The diffraction peaks corresponding to the hexagonal phase of $Ni(OH)_2$ are observed at $2\theta \approx 19.13^o$, 33.01^o, 38.31^o, 51.95^o, 58.80^o, 62.58^o, 69.74^o, 72.98^o and 82.70^o which are indexed to the (001), (100), (011), (012), (110), (111), (200), (201) and (202) crystal planes respectively. After calcination at 350 and 500 ^oC diffraction peaks appear at $2\theta \approx 37.16^o$, 43.18^o, 62.80^o, 75.30^o and 79.44^o. These peaks are indexed to (111), (200), (220), (311) and (222) respectively, corresponding to face-centered-cubic (fcc) structured NiO with lattice parameters of a = 0.4177 nm (space group: *Fm3m*, JCPDS file no. 78-0429). These results show that $Ni(OH)_2$ has decomposed completely at 350 ^oC into pure single phase nanocrystalline NiO. The crystallite sizes of the as-prepared and calcined samples were calculated from the major diffraction peaks, i.e. (011) of $Ni(OH)_2$ and (200) of NiO using the Debye-Scherrer formula. The crystallite sizes of as-prepared and calcined samples at 350 and 500 ^oC were found to be 16.4 nm, 12.6 nm and 19.8 nm respectively.

The thermal gravimetric analysis pattern for as-prepared powder is shown in Figure 3.3.2. The weight loss (about 17.3 mass %) in the region 210–350 ^oC is due to the removal of one water molecule which is associated with the thermal decomposition of $Ni(OH)_2$ to NiO [El-Kemaryn *et al.* (2013)]. There is no weight loss after 350 ^oC, confirming the formation of nanocrystalline NiO.

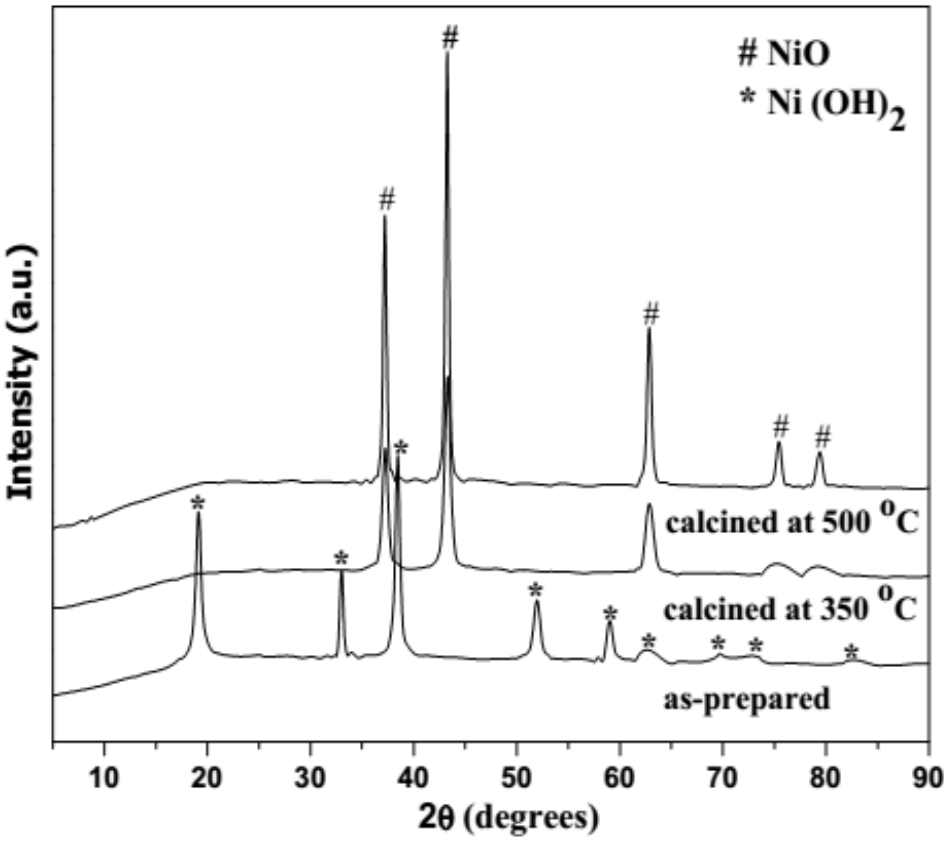

Figure 3.3.1. XRD patterns of as-prepared and calcined samples.

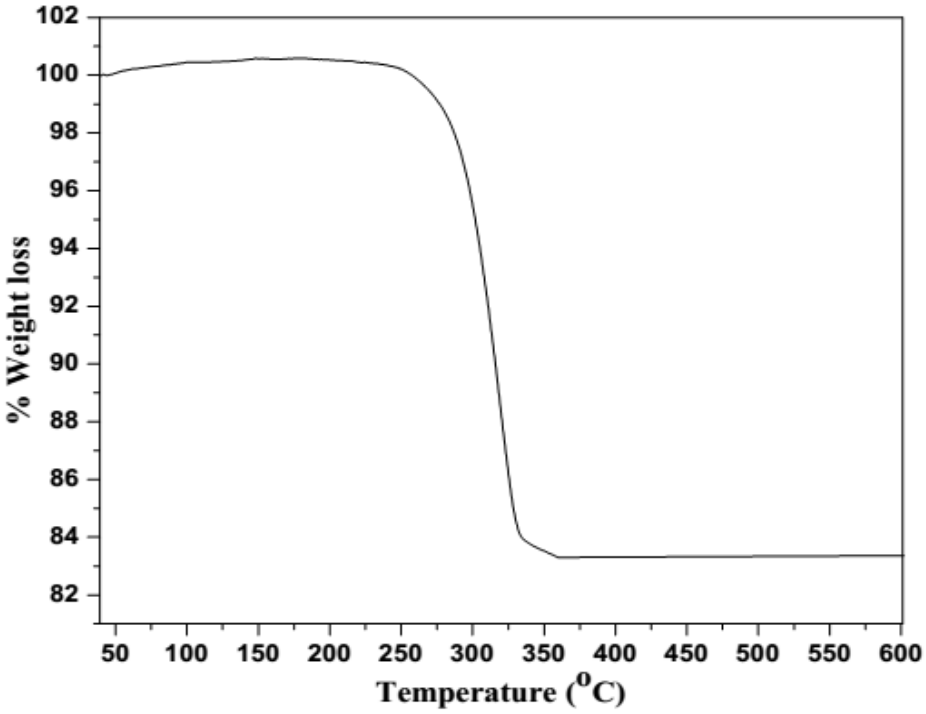

Figure 3.3.2. Thermal gravimetric analysis curve of as-prepared sample.

The FT-IR spectra of as-prepared and calcined samples are shown in Figure 3.3.3. The FT-IR spectra of as-prepared sample show peak at 3651 cm^{-1} corresponding to the stretching vibration (νO-H) of non-hydrogen bonded hydroxyl groups in the nickel hydroxide ($Ni(OH)_2$) [Saghatforoush *et al.* (2012)]. The broad absorption bands at 3437 and 1633 cm^{-1} are due to the moisture present in the KBr which is used for preparing the pellets in open air [Saghatforoush *et al.* (2012), Al-Sehemi *et al.* (2014), Kalam *et al.* (2013)]. The broad band at around 650 cm^{-1} is characteristic of the stretching vibration of hydroxyl groups in which hydrogen bonded to Ni–O [Al-Sehemi *et al.* (2014)]. The band at 519 cm^{-1} is assigned to the δ(O–H) vibration in the as-prepared sample [Kalam *et al.* (2013)]. The band appearing at 473 cm^{-1} is related to the Ni–O stretching vibration of octahedral NiO_6 in the cubic NiO structure [Christy and Umadevi (2013), Dam and Lee (2013)]. Thus FT-IR spectra are in agreement with the XRD patterns.

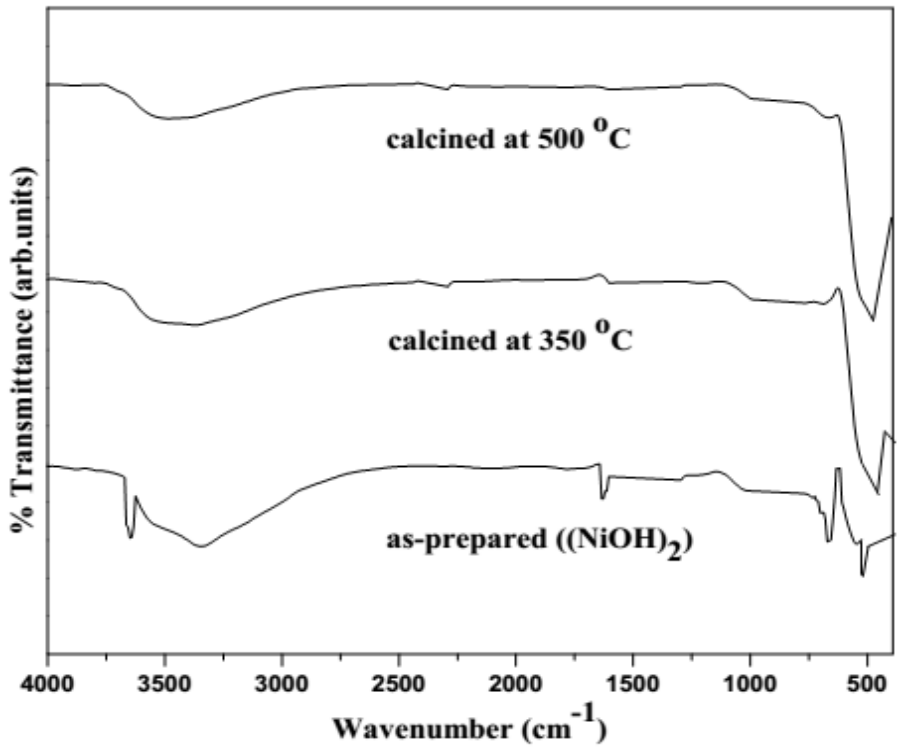

Figure 3.3.3. FT-IR spectra of as-prepared and calcined samples.

UV-Visible diffuse reflectance spectroscopy is one of the important methods to reveal the energy structures and optical properties of the semiconductor nanocrystals. Diffuse reflectance spectra of the samples calcined at 350 and 500 ^{o}C are shown in Figures 3.3.4(a) and 3.3.4(b). The calcined samples at 350 and 500 ^{o}C exhibit different absorption bands 340 nm and 363 nm respectively which are attributed to the nanocrystalline NiO [Thota and Kumar (2007), El-Kemaryn *et al.* (2013), Zhu *et al.* (2013)]. The optical band gap (Eg) of the nanocrystalline NiO was determined by employing Tauc relationship [Al-Sehemi *et al.* (2014)]. The plots between $(\alpha h\upsilon)^2$ on the y axis and photon energy ($h\upsilon$) on the x-axis are given in Figures 3.3.4(c) and 3.3.4(d) which are obtained from the data of Figures 3.3.4(a) and 3.3.4(b). The estimated band-gap energy, thus found, are 3.64 and 3.41 eV for nanocrystalline NiO calcined at 350 and 500 ^{o}C respectively which show red-shift compared to that of the bulk NiO (4.0 eV) [Zhu *et al.* (2013)]. This is due to quantum size effect, chemical defects or vacancies present in the crystal structure which generate a new energy level to reduce the band gap energy [Song and Gao (2008)]. Thus, as the calcination temperature or crystallite size of the nanoparticles increases the energy band gap of the semiconductor decreases (Table 3.3.1).

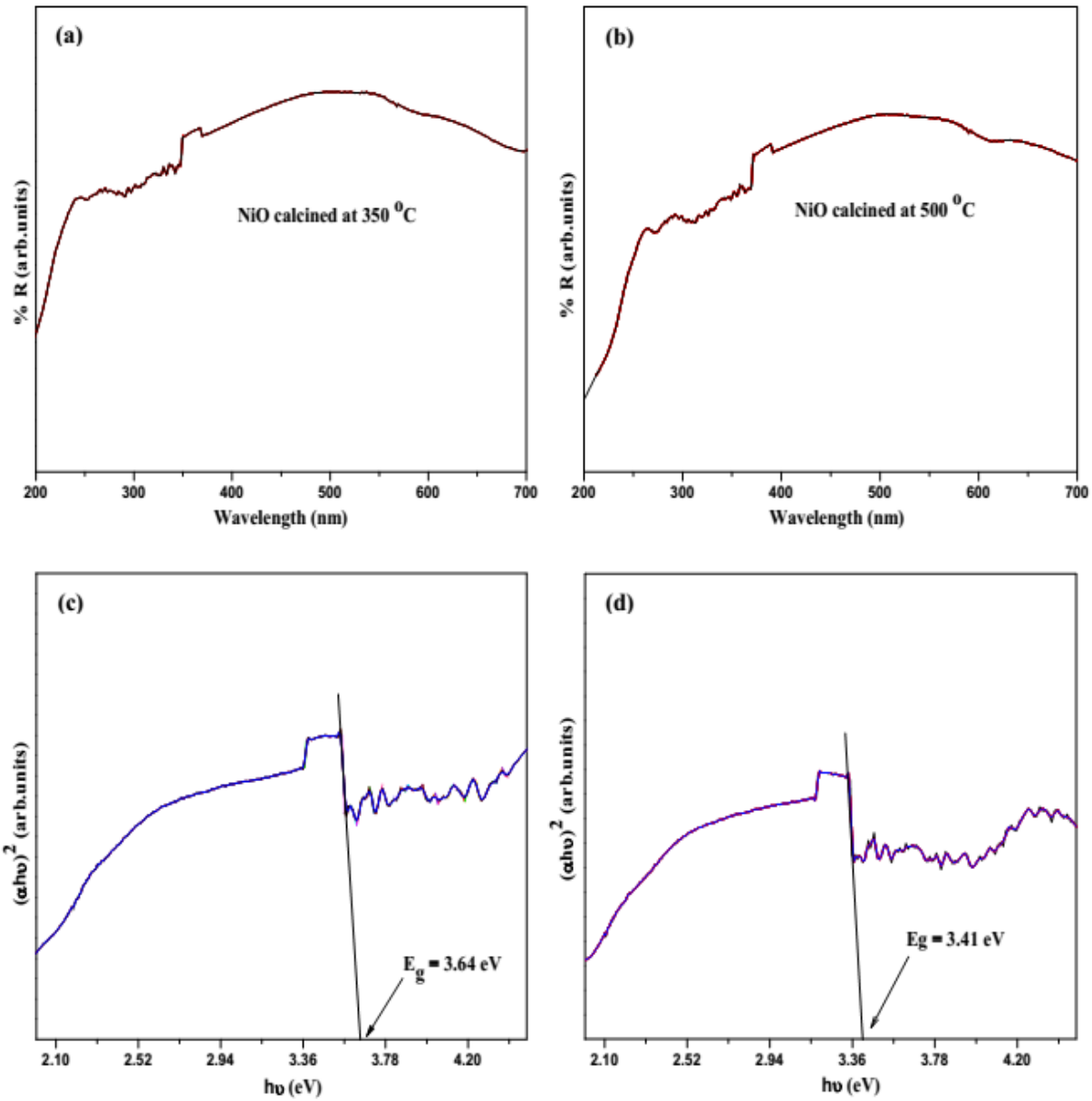

Figure 3.3.4. Diffuse reflectance spectra of nanocrystalline NiO: (a) after calcination at 350 ^{o}C, (b) after calcination at 500 ^{o}C, and the plot (c) and (d) for $(\alpha h\upsilon)^2$ versus $h\upsilon$ drawn from the data (a) and (b).

Table 3.3.1. Crystallite size and band gap values of nanocrystalline NiO calcined at 350 ^{o}C and 500 ^{o}C.

Sample	Crystallite size (nm)	Band gap energy (eV)
Nanocrystalline NiO calcined at 350 ^{o}C	12.6	3.64
Nanocrystalline NiO calcined at 500 ^{o}C	19.8	3.41

BET (Brunauer-Emmett-Teller) surface area measurements were carried out for the as-prepared and calcined samples (Table 3.3.2). The nitrogen adsorption–desorption isotherms onto the nanocrystalline NiO is shown in Figure 3.3.5(a). The isotherms resemble to the classical type IV isotherm of IUPAC classification [Al-Sehemi *et al.* (2014), Kalam *et al.* (2013)] indicating the presence of mesopores in the samples. The initial part of the Type IV isotherm (at low relative pressure ranges) is attributed to monolayer-multilayer adsorption since it follows the same path. The hysteresis loop starts at the relative pressure (P/Po) of about 0.5 and expands almost to 1.0, indicating the complete filling of the mesopores. By using the BJH plot of adsorption branch in Figure 3.3.5(b), the pore size distribution of the nanocrystalline NiO calcined at 350 and 500 ^{o}C are obtained as 4.3 and 5.6 nm respectively. The presence of porous structures in the NiO samples is beneficial for the enhancement in catalytic performance due to the easy diffusion of the reactants and facile accessibility of the active sites [Bai *et al.* (2013)]. The BET results indicate that nanocrystalline NiO calcined at 350 ^{o}C has high specific surface area (162.8 m^2g^{-1}) and total pore volume (0.18 cm^3 g^{-1}) compared to the as-prepared $Ni(OH)_2$ (SSA ~ 108.6 m^2g^{-1} and TPV ~ 0.15 cm^3 g^{-1}). Further, calcination at 500 ^{o}C results in the fast removal of hydroxyl species which causes a decrease in the specific surface area and total pore volume to 98.7 m^2g^{-1} and 0.13 cm^3 g^{-1} respectively. The

specific surface area of NiO nanoparticles synthesized by other methods like the anodic arc plasma [Wei *et al.* (2009)], chemical precipitation [Behnajady and Bimeghdar (2014)] and microwave combustion methods [Manikandan *et al.* (2013)] are about 33 m^2g^{-1}, 71.1 m^2g^{-1} and 73.5 m^2g^{-1} respectively which are appreciably lower than that obtained in the present method.

Table 3.3.2. BET surface area and pore volume of as-prepared and calcined samples.

Sample	Surface area (m^2 g^{-1})	Pore volume (cm^3 g^{-1})
As-prepared ($Ni(OH)_2$)	108.6	0.15
Nanocrystalline NiO (calcined at 350 ^oC)	162.8	0.18
Nanocrystalline NiO (calcined at 500 ^oC)	98.7	0.13

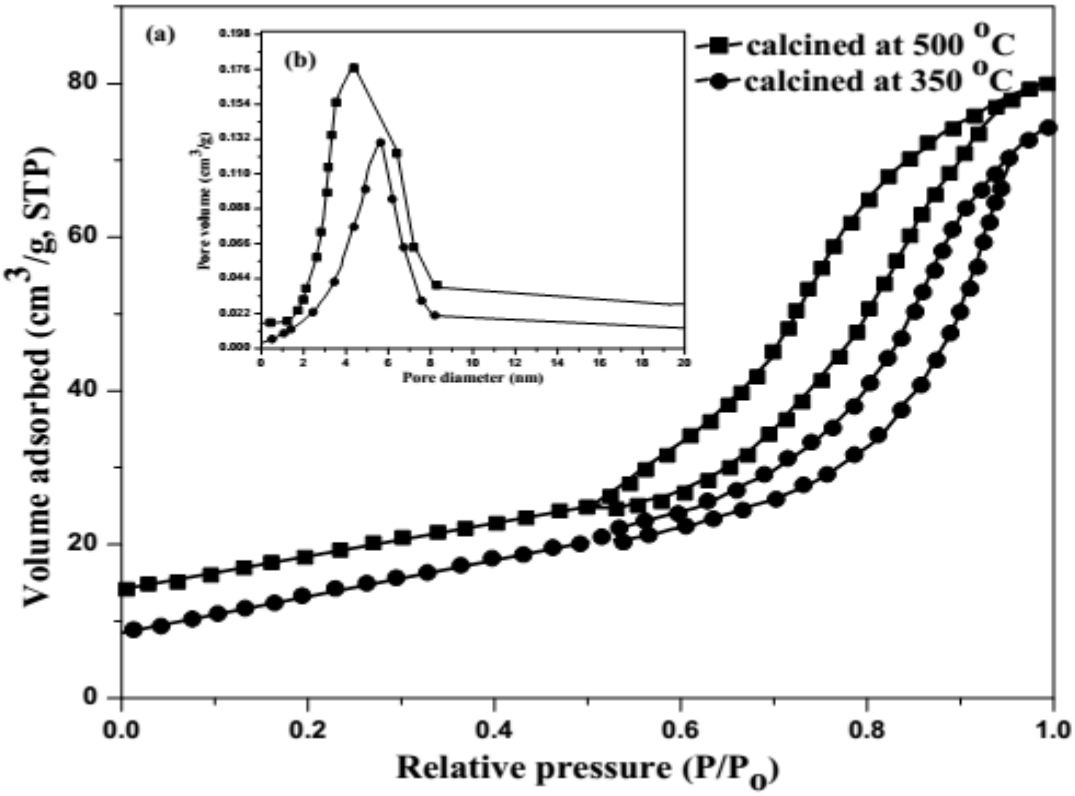

Figure 3.3.5. (a) N_2 adsorption-desorption isotherms and (b) pore-size distribution of nanocrystalline NiO.

FE-SEM images of the samples (before and after calcination) in different magnifications are shown in Figures 3.3.6 and 3.3.7. The FE-SEM images show that the as-prepared $Ni(OH)_2$ consists of a large number of nanoflakes-like structures with thickness of about 26 ± 3 nm (Figures 3.3.6a and 3.3.7a). Nanoflakes-like morphology of as-prepared $Ni(OH)_2$ changes to porous sheet-like structures of NiO (thickness: ~ 20 ± 2) on calcination at 350 ^oC (Figures. 3.3.6b and 3.3.7b). On calcination at 500 ^oC, these porous sheet-like structures of NiO get converted to porous NiO with hexagonal sheet-like morphology (Figures 3.3.6c and 3.3.7c). On calcination at 500 ^oC the complete formation of hexagonal sheet-like morphology takes place. The conversion of $Ni(OH)_2 \rightarrow NiO$ is accompanied by a volume contraction and the intrinsic crystal contraction has a highly porous structure. Figure 3.3.6(d) shows the EDXA spectrum indicating the presence of only nickel and oxygen elements. On the basis of the elemental analysis data of the samples, the atomic ratio of nickel to oxygen in as-prepared sample is 0.50 and in calcined samples at 350 and 500 ^oC they are 0.98 and 1.01, respectively (Table 3.3.3). The EDX analysis data confirmed the presence of high purity nanocrystalline NiO after calcination.

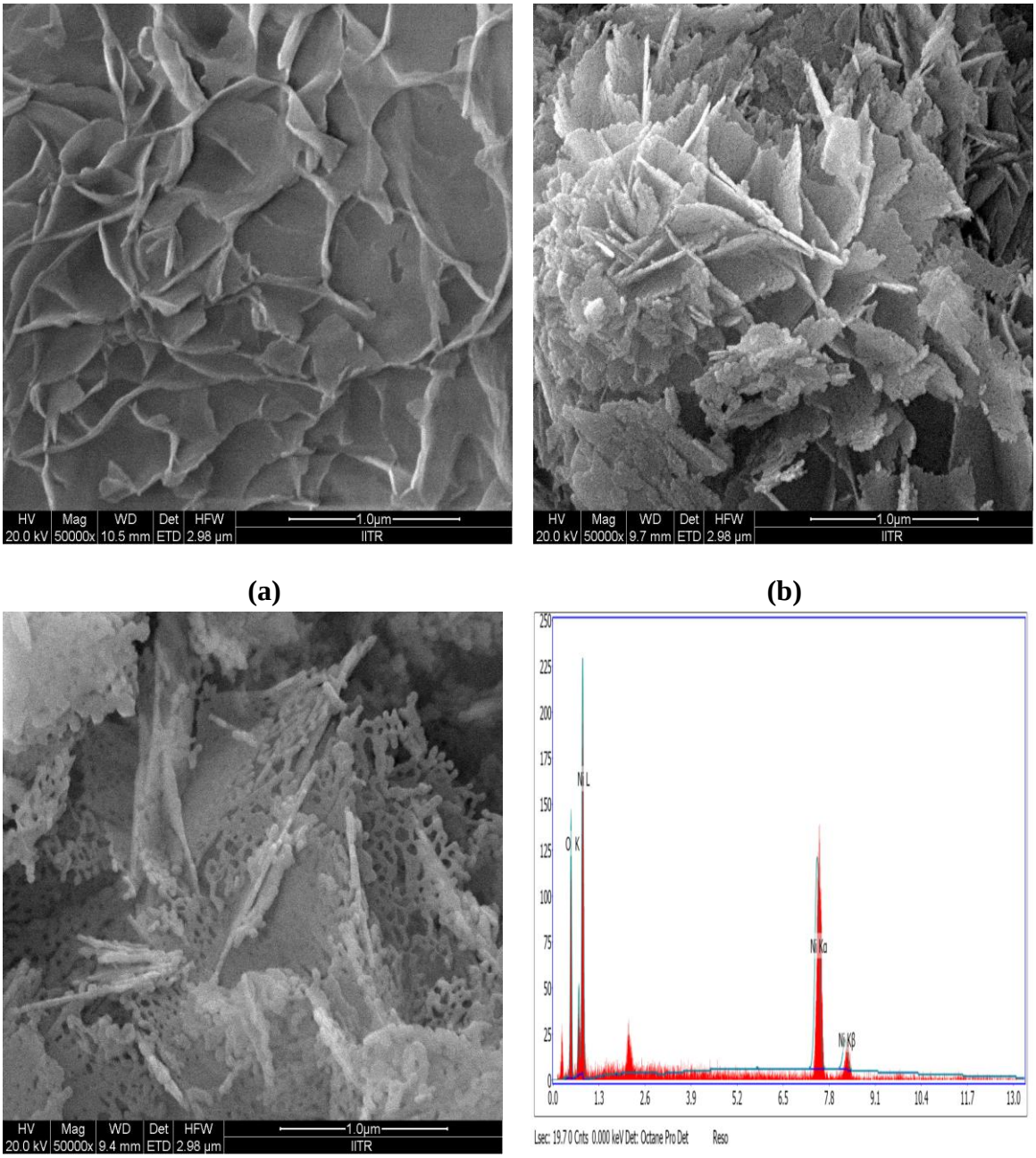

Figure 3.3.6. FE-SEM images of samples at low magnification: (a) as-prepared, (b) calcined at 350 ^{o}C, (c) calcined at 500 ^{o}C, and (d) EDX analysis plot of nanocrystalline NiO.

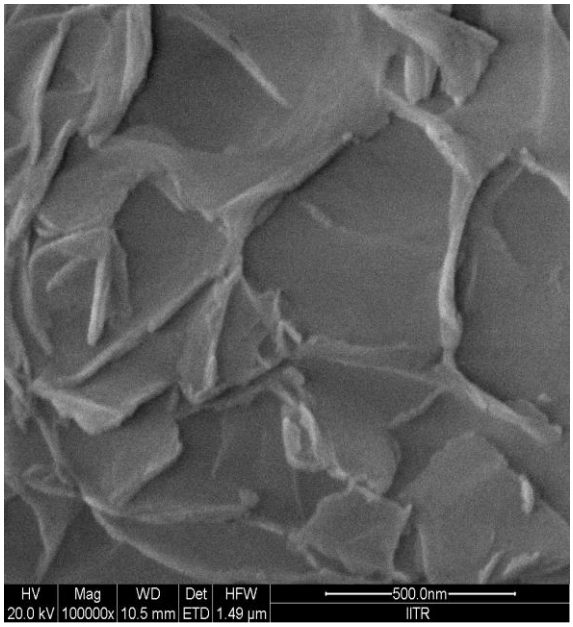

(a)

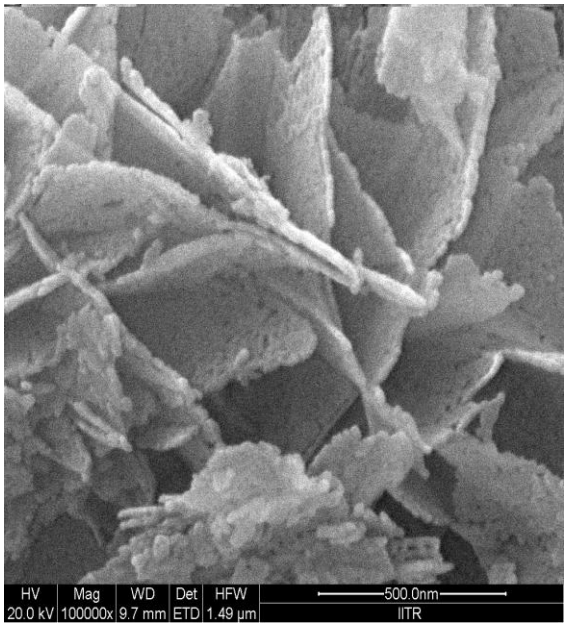

(b)

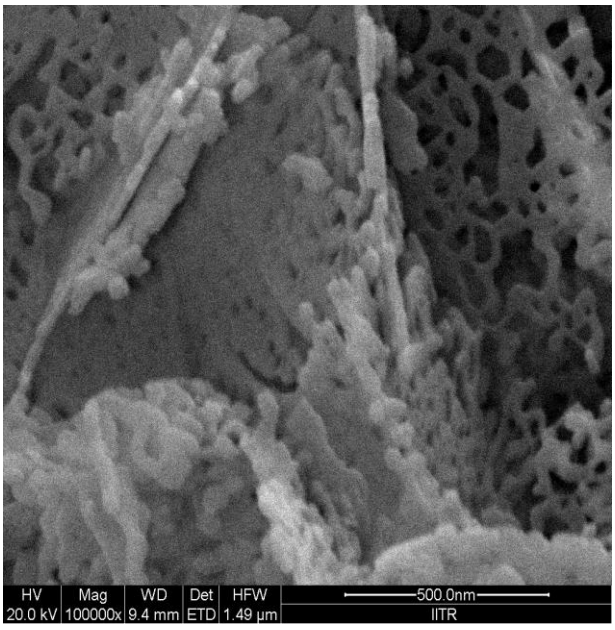

(c)

Figure 3.3.7. FE-SEM images of samples at high magnification: (a) as-prepared, (b) calcined at 350 ^{o}C, and (c) calcined at 500 ^{o}C.

Table 3.3.3. EDXA data of as-prepared and calcined samples.

Sample	Element	At%	Wt%	Ni/O
As-prepared	Ni O	29.26 57.74	56.57 30.43	0.50
Nanocrystalline NiO calcined at 350 ^{O}C	Ni O	55.46 56.54	78.26 21.74	0.98
Nanocrystalline NiO calcined at 500 ^{O}C	Ni O	50.28 49.72	78.77 21.23	1.01

TEM image of the as-prepared sample calcined at 500 ^{o}C is shown in Figure 3.3.8(a). It was observed that the nanocrystalline NiO obtained on calcination at 500 ^{o}C exhibits porous hexagonal sheet-like morphology. The mean particle size of nanocrystalline NiO estimated from TEM measurement was 21.4 ± 0.2 nm which is in accordance with the powder X-ray diffraction results. The selected-area electron diffraction (SAED) pattern of the NiO nanoparticles is shown in Figure 3.3.8(b). The clear rings with superimposed bright spots indicate the presence of nanocrystalline NiO. The SAED results are in good agreement with XRD measurements.

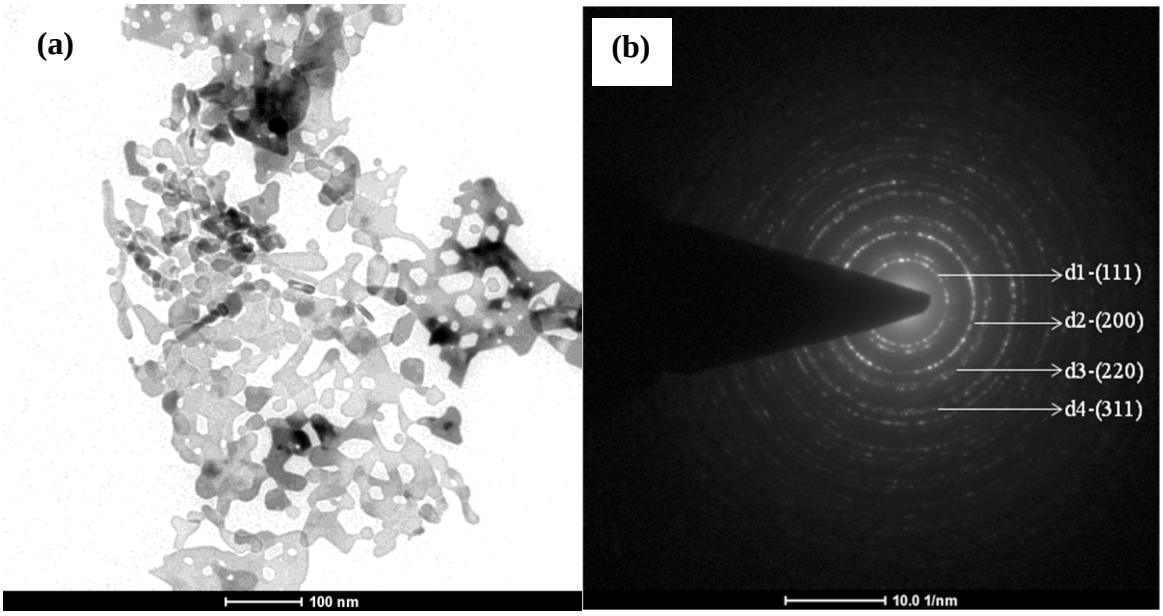

Figure 3.3.8. (a) Typical TEM image and (b) corresponding SAED pattern of nanocrystalline NiO.

In the present study, the synthesized samples were tested for their catalytic activity for the reduction of 4-nitrophenol to 4-aminophenol using sodium borohydride at room temperature. The reduction of 4-nitrophenol with $NaBH_4$ was also carried out in the absence of catalyst. The time required for complete conversion of 4-nitrophenol to 4-aminophenol was observed by decolorization of yellow colour of 4-nitrophenol which is summarized in Table 3.3.4. From the Table 3.3.4 it is inferred that the reduction of 4-nitrophenol does not take place either in the absence of the catalyst or in the presence of as-prepared $Ni(OH)_2$. The proposed mechanism [Mandlimath *et al.* (2011), Solanki and Murthy (2011), Chiou *et al.* (2013)] for catalysis is that first adsorption of 4-nitrophenol as well as BH_4^- ions take place on the surface of the nanocrystalline NiO (Figure 3.3.9). Then, nanocrystalline NiO mediate the electron transfer from the donor species (BH_4^- ions) to the acceptor species (NO_2 group) with the formation of 4-aminophenolate ions, followed by its desorption from the surface of the catalyst. Generally, nanocatalytic materials with a high surface area provide the materials with better catalytic activity [Zhu *et al.* (2007)]. In Table 3.3.4, sample calcined at 350 ^oC exhibits a higher catalytic activity for the reduction of 4- nitrophenol than that calcined at 500 ^oC, which is in accordance with their specific surface area 162.8 $m^2\ g^{-1}$ (at 350 ^oC) and 98.7 $m^2\ g^{-1}$ (at 500 ^oC). Samples with high surface- to -volume ratios facilitate many active sites for the catalysis. The nanocrystalline NiO serves as a better catalyst for the reduction of 4-nitrophenol (time of reduction: 18 to 22 min) as compared to the reported result of Bayal and Jeevanandam (2012a) (time of reduction: 34 min).

Table 3.3.4. Time required for the complete reduction of 4-nitrophenol in the presence of synthesized samples as catalyst.

S. No.	Reaction condition	Time required for the reduction (min)
1.	4-Nitrophenol + $NaBH_4$	No reduction
2.	4-Nitrophenol + $NaBH_4$ + as-prepared sample ($Ni(OH)_2$)	No reduction
3.	4-Nitrophenol + $NaBH_4$ + NiO calcined at 350 ^oC	18
4.	4-Nitrophenol + $NaBH_4$ + NiO calcined at 500 ^oC	22

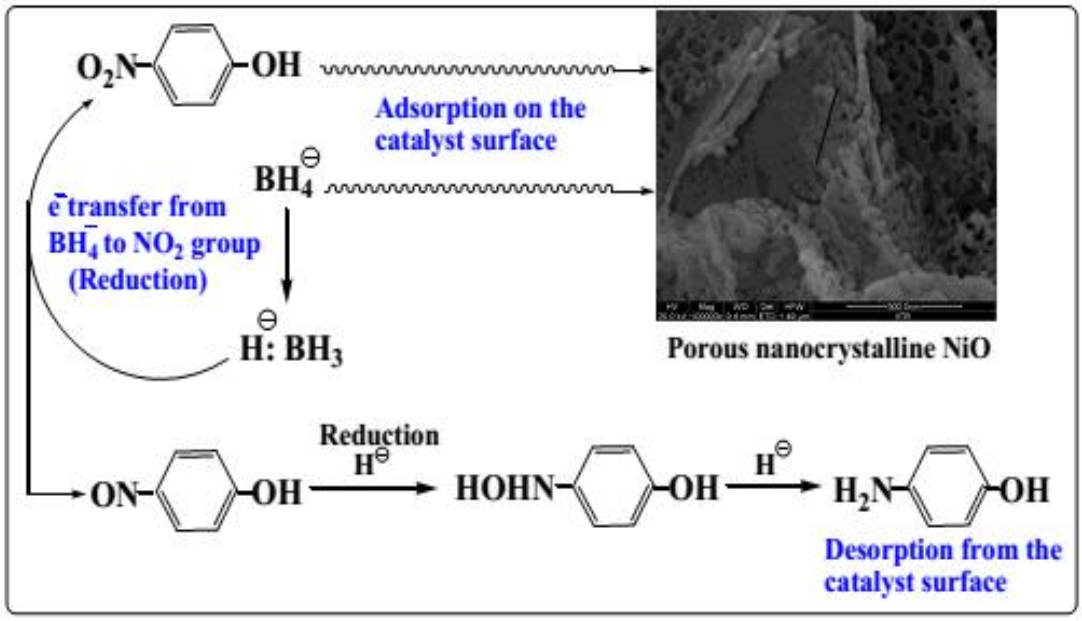

Figure 3.3.9. Schematic diagram representing the mechanism for the reduction of 4-nitrophenol to 4-aminophenol in the presence of nanocrystalline NiO.

3.4. Conclusions

Nanocrystalline CuO with dandelion-like morphology was successfully prepared by a simple homogeneous precipitation method at low temperature (~ 80 ^oC) in short precipitation time without using any surfactant or microwave irradiation. The samples were characterized using various analytical techniques. From XRD observation it is

evident that monophasic and highly crystalline monoclinic CuO is only forming. TGA pattern indicates that there is no weight loss above 400 ^{o}C, the calcination temperature. The formation of nanocrystalline CuO is confirmed by FT-IR studies. It is observed from the FE-SEM images that there is an increase in average size of microspheres of CuO from 1.73 ± 0.14 μm to 3.35 ± 0.22 μm on increasing the calcination temperature. Also, with the increase in calcination temperature the atomic ratio of copper to oxygen increases showing the purity of nanocrystalline CuO on the basis of EDX analysis. Moreover, this method may be extended to large scale synthesis of other transition metal compounds. The catalytic activity of the nanocrystalline CuO powder was determined by carrying out the reduction of 4-nitrophenol to 4-aminophenol with $NaBH_4$ at room temperature. The studies indicate that the nanocrystalline CuO powder acts as a better catalyst than the earlier reported work because of its high surface- to -volume ratios which facilitate many active sites for catalysis.

ZnO-NPs have been successfully synthesized by a simple homogeneous precipitation method without using any surfactant, chelating or gelating agents in short time and at low calcination temperature. The samples were characterized using a variety of analytical techniques. The calcination temperature strongly influences the morphology, specific surface area and pore volume. ZnO-NPs having high surface area go along with small particle size exhibit stronger antifungal activity. The antifungal activity of ZnO-NPs was tested against pathogenic *Candida albicans* by disc diffusion susceptibility method. It is observed that, on increasing the ZnO-NPs concentration, zone of inhibition also increases. In future, the antifungal activity study of ZnO-NPs will be extended to other fungal and bacterial strains.

Porous nanocrystalline NiO with hexagonal sheet-like morphology was successfully synthesized by a simple homogeneous precipitation method at low calcination

temperature in large scale. The method is an easy way to prepare nanocrystalline NiO in short precipitation time without using any surfactant, chelating or gelating agent. The samples were characterized by means of an array of analytical techniques. The calcination temperature is an important factor to affect strongly the morphology, specific surface area, pore volume and optical band energy of the samples. The optical band gap value of nanocrystalline NiO decreases on increasing the calcination temperature. The surface area measurements indicate that the nanocrystalline NiO obtained under homogeneous precipitation method has high surface area. Catalytic activity of the nanocrystalline NiO powder was tested for the reduction of 4-nitrophenol to 4-aminophenol. It is inferred from the present studies that the synthesized porous nanocrystalline NiO powder acts as a better catalyst compared to earlier work.